Uncertainty Quantification of the Neutronics Model of the U-Battery with Reduced Models

by

Erik van den Broek

to obtain the degree of Master of Science
at the Delft University of Technology,
to be defended publicly on Friday August 26, 2022 at 9:00.

Student number:	4466764	
Project duration:	October 11, 2021 – July 31, 2022	
Thesis committee:	Dr. Z. Perkó,	TU Delft, supervisor
	Dr. ir. D. Lathouwers,	TU Delft
	Prof. dr. ir. J. L. Kloosterman,	TU Delft

TU Delft

Abstract

High-fidelity models are computationally intensive to work with in many-query applications, such as the design process of small modular reactors. A reduced order model of the high-fidelity model can still accurately determine the quantities of interest with only a fraction of the computational cost, and thus can potentially solve the aforementioned problem. However, reducing a high-fidelity model of a small modular reactor is complicated due to the large number of parameters involved in nuclear reactor models, as that leads to an exponentially increasing parameter space needed to be surveyed.

Disregarding the parameters with the smallest impact on the output and thereby reducing the total number of variables can limit the parameter space, and thus speed up the model reduction at the cost of some accuracy. Perturbation theory utilizes the benefits of adjoint theory to efficiently determine sensitivities of responses to all the variables in the model, which allows one to find the influence on the output of the different variables without the need for evaluating them all repeatedly. It is then possible to apply a reduced order modeling technique such as proper orthogonal decomposition to determine and select only the most important eigenmodes of the high-fidelity model and build a reduced model.

This approach is applied to three different neutronics model of the U-Battery, varying in complexity. The presented method has shown to alleviate computational cost significantly for all examined reduced models. However, the upfront cost of building the reduced models by sampling the high-fidelity models has been considerable, especially when evaluating the resulting accuracy of the reduced models. A proper selection of the proper orthogonal decomposition tolerances must be made to ensure sufficient accuracy and to prevent oversampling. Nonetheless, combining proper orthogonal decomposition with perturbation theory showed to be a promising way of selecting only a few parameters for participation in the building of reduced order models while minimizing the loss of accuracy compared to the high-fidelity model.

Acknowledgements

Foremost, I would like to express enormous gratitude to all the help from Zoltán Perkó, for the abundance of meetings, for the ever remaining interest in my progress each week, and for his continuous guidance. Furthermore, I would like to thank Marc van den Berg for the insightful discussions on the models and the results, and Danny Lathouwers for his help with getting PHANTOM-S_N to run. I would also like to thank Quint van Velthoven for his supporting role in understanding the struggles of a Master's thesis and for his help with reviewing the thesis. In addition, I want to thank all members of the RPNM group for their contribution to the many joyous lunches and walks. Finally, I would like to thank my parents for their endless support and my friends for the much-needed distractions during the whole project.

Erik van den Broek
Delft, July 2022

Contents

Chapter 1

Introduction

In the current worldwide energy crisis, there is a need to transition towards sustainable ways to produce energy, foremost, to prevent emissions of green house gasses and to prevent further detrimental damage to the environment due to climate change [1]. Another important, geopolitical, reason to transition from fossil fuels has become more noticeable lately in Europe. The heavy reliance on fossil fuels comes hand in hand with a reliance on the countries that provide the needed fuels, and sustainable solutions take away the pressure of the dependence on other nations [2]. Moreover, the sustainable methods have become a cost competitive option as well [3].

While solar and wind energy are much needed for a complete transition from fossil fuels, they still come with a few problems that limit their widespread usability. They cannot produce energy in a constant manner, even though there always is a demand. A baseload is needed to prevent circumstantial loss of energy availability, which is commonly provided by fossil fueled power plants [4]. Furthermore, it takes a long time and a large investment to build the infrastructure for these options in remote places or developing countries [5]. Developed countries are having troubles with solar and wind farms as well, due to aging electric grids causing outages or getting fully used too quickly, leaving no room for new grid users [6].

A solution to these problems is the use of nuclear energy in the form of small modular reactors (SMRs). As opposed to large-size nuclear reactors, SMRs are easily transportable by rail, barge or truck, and this ease of transportation makes the use of SMRs in more places possible, as their flexibility reduces the dependence on infrastructure [7]. In addition, they do not require a high capital investment, which increases their usability for sites where the energy need is limited. Moreover, their modularity enables larger industrial users to transition away from fossil fuels and simultaneously avoid straining the energy grid.

A key advantage of SMRs compared to the conventional large-size nuclear power plants is their potential to be inherently safe. Reactor designs for SMRs have been proposed that rely on passive cooling methods during normal operation or accidents, which is made possible by their commonly lower operating temperatures [8]. The reactor core can then be passively cooled in all operational conditions [8].

To ensure safe use of a particular reactor design during all operating conditions and throughout its whole lifetime, numerical models are necessary. They represent the reactor in simulations, and are used for the first design steps and further optimization. These models require a high-fidelity to reflect reality as accurately as possible. Still, the most accurate models produce outputs over a varying range of possible results, because there are uncertainties tied to the geometry, material properties and other variables of the model. The uncertainties are propagated through the model and cause the results to contain uncertainties as well [9]. The quantification of the uncertainty is a requirement to ensure the safety of the reactor [10].

The design, optimization, and uncertainty quantification steps lead to the need for many evaluations of the high-fidelity model. High-fidelity models are, however, costly to compute with, both in time and resources. It becomes unmanageable to evaluate them for the multitude of parameter settings needed for all the modeling steps [11]. As the number of evaluations required for uncertainty quantification alone can range in the hundreds of thousands, another method of evaluating high-fidelity models needs to be used. An alternative approach is to determine the

reduced order model (ROM) of the high-fidelity model using mathematical methods, which can still accurately determine the quantities of interest with only a fraction of the computational cost [12]. To that order, we use proper orthogonal decomposition (POD) as our ROM technique [13].

Another problem in nuclear reactor simulations is the large number of variables involved. For each nuclide present, either part of the fuel, reflector, control rod or structural material, nuclear data in the form of cross sections are needed. As the geometry becomes more detailed in a high-fidelity model, the number of nuclides will increase. In addition, the nuclear data is energy dependent and increasing the energy resolution adds more cross section data to each nuclide. The problem gets out of hand when trying to build a reduced model, as we want to survey the parameter space of the model by evaluating the input variables at different parameter settings. Due to the curse of dimensionality, the parameter space that will need to be analyzed increases exponentially for an increasing number of variables [7].

To lessen the exponential grow, the parameters with the smallest impact on the output of the model can be disregarded, reducing the total number of variables. To know the influence of each individual variable on the quantity of interest, or response, would still require many evaluations. A workaround used in this work is generalized perturbation theory (GPT), which utilizes the benefits of adjoint theory to determine sensitivities of responses to all the variables in a much more efficient way [15].

1.1 U-Battery

The SMR considered in this work is the U-battery, a block-type high temperature reactor, where each hexagonal fuel block is loaded with TRISO coated fuel particles and is gas-cooled with helium. Around the fuel blocks are reflector elements, and the core of the reactor is surrounded by a thermal shield, a barrel, and a gas gap where the coolant can flow up. The whole assembly is surrounded by a reactor pressure vessel (RPV) and shown in a schematic overview in Figure 1.1.

The fuel assemblies are made of a graphite moderator and contain coolant channels, holes for the fuel pellets, and possibly fixed burnable poison rods. The TRISO particles consist of a low enriched uranium dioxide (UO_2) core, and four layers to form a strong encapsulation of the fuel

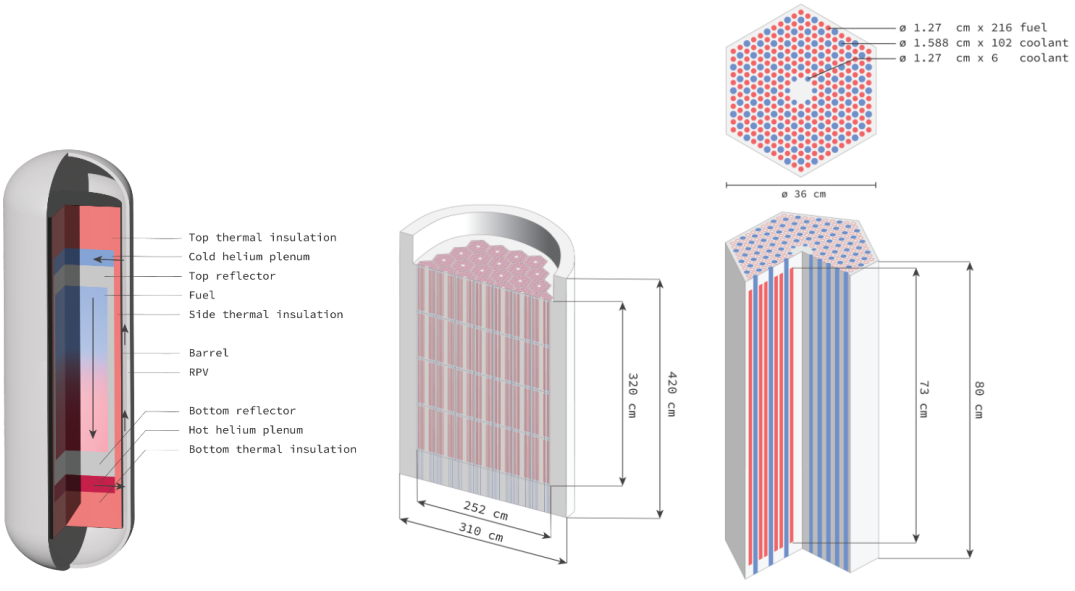

Figure 1.1: Schematic overview of the U-Battery design [14].

Table 1.1: Basic parameters of the U-Battery [8].

Parameter	Value
Reactor type	Block-type HTR
Lifetime	10 years
Thermal power	20 MW
System pressure	4 MPa
Inlet/outlet temperatures	250/750 °C
Mass flow rate	7.64 kg/s
Coolant	Helium
Fuel type	UO_2, TRISO coated particles
Fuel enrichment	12 %
Packing fraction TRISO particles	0.3

and act as a small pressure vessel. A schematic of a particle is illustrated in Figure 1.2. The first buffer layer of porous carbon is to capture fission products, while the next inner pyrolytic carbon, silicon carbide, and outer pyrolytic carbon layers are to maintain the structural integrity of the pellet. The fuel blocks can be assembled in varying ways, with the limitation of a maximum diameter of the RPV of 3.5 m, to allow transportation in a standardized shipping container. The particular design modeled in this work contains 4 planes of blocks stacked on each other, and 37 blocks per plane. The top and bottom reflector are both 50 cm, and the side reflector is 29 cm. Further basic parameters are summarized in Table 1.1.

1.2 Goals and structure

In this work, a solution is presented to the problems of the high computational cost involved with many-query applications of high-fidelity models, and the complication of the numerous parameters involved in nuclear reactor models, which leads to an exponentially increasing parameter space needed to be surveyed. The approach is applied to the neutronics model of the U-Battery. First, the most important variables of the high-fidelity model are determined using the GPT approach, after which a ROM is built for only these important variables. With the ROM, further analysis can be performed on the design without much computational effort.

The thesis is structured in the following way. Firstly, the theoretical background is given in Chapter 2. Chapter 3 follows with a description of the different models that are analyzed, and the codes that have been used to model the neutronics and that have been applied to build the reduced model. The results of the simulations and the analysis performed with the reduced models are presented in Chapter 4, which are subsequently discussed in Chapter 5. Finally, the conclusion is given in Chapter 6.

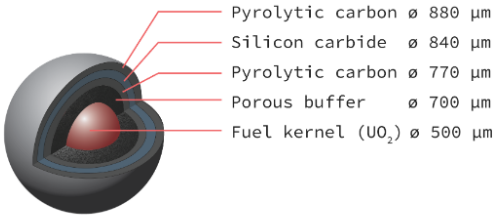

Figure 1.2: Schematic of a TRISO fuel particle [14].

Chapter 2

Theory

In this chapter, the theoretical background is given for the topics of this work. The concept of solving high-fidelity models numerically with the use of the Finite Element Method is shown in Section 2.1. Section 2.2 introduces the general ideas of the different techniques for reduced order modeling. Lastly, perturbation theory is explained in Section 2.3, from the basic need to efficiently determine response perturbations to the use of adjoints for any generalized perturbation.

2.1 Finite Element Method

A mathematical model consists of a domain, the representation of the real-life geometry, and equations that are solved on the domain. Solving a problem exact, or analytically, becomes prohibitively difficult for systems with a complex geometry. Instead, the numerical method of finite elements is used, where the equations are not solved on the single large domain, but on many small elements [16]. For each individual element, the equations are numerically integrated, and the numerical integration error remains low due to the elements being small. In this method, the solution $u(\boldsymbol{x})$ is approximated as a sum of coefficients u_j and linear basis functions $\phi_i(\boldsymbol{x})$, as shown in Equation (2.1), with n the number of nodes that form all the elements.

$$u^n(\boldsymbol{x}) = \sum_{j=1}^{n} u_j \phi_j(\boldsymbol{x}). \tag{2.1}$$

To determine the basis functions and the numerical integrations, the domain is first divided into a number of smaller elements. In a two-dimensional geometry, or in $\mathbb{R}^2$, the elements can be triangles, and the collection of elements is called a mesh. The subdivision into elements is shown in Figure 2.1 for the top part of the U-battery model, which has a cylindrical shape.

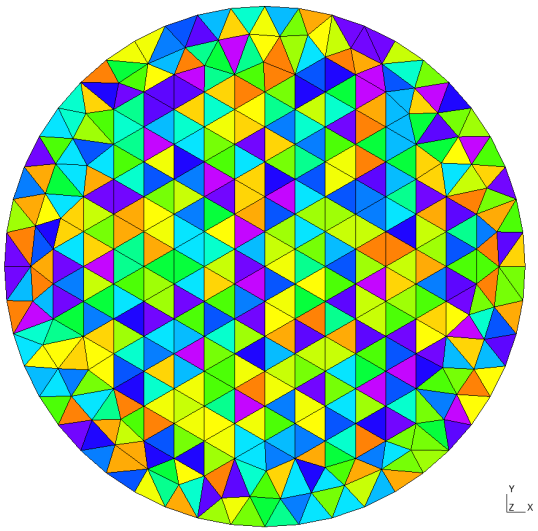

Figure 2.1: Subdivision into triangular elements of the top of the U-Battery model.

In $\mathbb{R}^2$, the triangular elements have three vertices, or nodes, $\boldsymbol{v_1}$, $\boldsymbol{v_2}$ and $\boldsymbol{v_3}$, which are the points that form the triangles. A basis function ϕ_i is defined on each node with the following properties:

$$1)\ \phi_i(\boldsymbol{x}) \text{ is linear per triangle,}$$
$$2)\ \phi_i(\boldsymbol{v_j}) = \delta_{ij},$$

with δ_{ij} the Dirac delta function. Such a linear basis function is shown in Figure 2.2. The node on which the basis is defined has a maximum value of one, while the basis function is linear on adjacent elements. The basis function is zero on elements that do not contain the corresponding node.

With the basis functions defined, the coefficients $\boldsymbol{u}$ can be determined by solving the equation in its numerical form, as shown in Equation (2.2).

$$S\boldsymbol{u} = \boldsymbol{f}. \tag{2.2}$$

The elements of S and $\boldsymbol{f}$ contain the numerical form of the equations, which depends on the operations in the equations.

The system of equations in Equation (2.2) can be solved efficiently with the use of a computer due to the possibility of using parallelization. However, a high-fidelity model has exceedingly small elements as to reduce the numerical error, which in turn needs more elements to fill the domain. As the set of equations is proportional to the number of elements, this comes with a larger computational cost to solve. The number of elements can be called the dimensionality of a model, and can range into the hundreds of thousands for fine detailed models. It becomes unsuitable for many-query applications to use such high-fidelity models, which leads to the introduction of reduced order models that can lower the dimensionality of a complex model.

2.2 Reduced Order Modeling

Reduced order modeling is a mathematical method that lowers the dimensionality of a full order model, which strongly reduce the resources required to get a solution for a complex model. The methods seek a reduced model that is not only much more efficient to solve, but which can approximate the full order model accurately as well. These properties make reduced models instrumental in solving the problem of evaluating high-fidelity models repeatedly. There are a number of different techniques that can reduce the order, or dimensions, of a model, which can be divided broadly into three categories, namely hierarchical, projection-based and data-fitting methods [18].

Hierarchical methods use a variety of tools to go from the full order model with high fidelity towards a lower fidelity model, such as simplifying assumptions, coarser computational grids or relaxed tolerances. The models with different fidelities can then be used cooperatively, leading to a multifidelity approach.

Projection-based techniques construct a reduced basis upon which the model equations are projected. The dimensionality of the model gets reduced as the reduced equations have a smaller dimensionality after the projection. Projection-based techniques differ in how they determine the reduced basis, and a number of techniques have been constructed [12]. One way to find the reduced basis is by using proper orthogonal decomposition (POD), which determines the eigenmodes of a system and selects the most important ones. This selection for the basis minimizes the error that is introduced when the other, less important, modes are truncated.

Consider, for example, a general linear differential equation where the parameters are gathered in the vector α,

$$\frac{\mathrm{d}y(\alpha)}{\mathrm{d}\alpha} = Ay(\alpha) + Bu(\alpha), \tag{2.3}$$

where $y(\alpha) \in \mathbb{R}^n$ gives the solution of the system with n dimensions, $u(\alpha)$ is the input signal, and A and B are the matrices of the discretized linear operator and input, respectively.

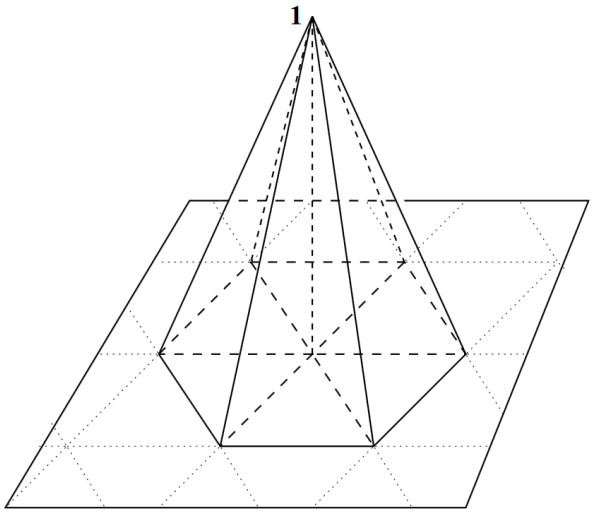

Figure 2.2: A single linear basis function on a two-dimensional mesh [17].

The solution can be approximated as

$$y(\alpha) \approx y_r(\alpha) = Vz(\alpha), \tag{2.4}$$

where the reduced basis spans the columns of V, such that $z(\alpha) \in \mathbb{R}^r$ with $r \ll n$. With the help of a projection matrix W, defined such that $W^TV = I$, where I is the identity matrix, the differential equation can be projected upon the reduced basis:

$$\frac{\mathrm{d}z(\alpha)}{\mathrm{d}\alpha} = A_r z(\alpha) + B_r u(\alpha), \tag{2.5}$$

where $A_r = W^TAV$ and $B_r = W^TB$ are the reduced forms of the original matrices. As the dimensions of the system have decreased significantly, computations with the reduced model are faster. In addition, the dynamics of the original system will be captured effectively if an appropriate basis is chosen, which would make the reduced model accurate as well.

The third category uses *data-fitting* to build the reduced model. This approach is able to form a surrogate model using only the output data at varying parameter settings. The original model is first written as a combination of unknown basis functions

$$y(\alpha) = \sum_{i=1}^{n} c_i(\alpha)\boldsymbol{u}_i, \tag{2.6}$$

where α is again the parameter vector, and $c_i(\alpha)$ are the coefficients of the basis vectors $\boldsymbol{u}_i$ [19]. Instead of projecting the original equations upon the reduced basis, methods such as interpolation or regression are used to calculate the coefficients in Equation (2.6). The reduced model can again be constructed with the POD technique, using only the basis vectors associated to the r most important eigenmodes:

$$y(\alpha) \approx y_r(\alpha) = \sum_{i=1}^{r} c_i(\alpha)\boldsymbol{u}_i. \tag{2.7}$$

While the first two types of techniques requires access to the full model equations, which is an intrusive way of modeling, data-fitting is able to produce a reduced model without any knowledge of the original model [20]. Such black-box modeling is a nonintrusive method and is essential in cases where the original equations are not readily available. Another reason for preferring a nonintrusive ROM technique is their widespread applicability due to their ease of

application. Projecting the full system equations onto a reduced basis requires manually including and adapting these equations into the code that produces the ROM for every individual system. A nonintrusive technique, however, needs less adaptation of the original system and can therefore be applied easier. In this work, the code used to solve the models is difficult to modify, such that a nonintrusive technique is a necessity.

One more important point to look at is the ability of a ROM method to produce a model for nonlinear systems. Some methods are only valid for linear equations and need linearization to work with nonlinear models. Such methods are therefore not preferred for highly nonlinear systems. POD is one of the methods that is valid for nonlinear models [19], and is, combined with the capability to be nonintrusive, hence the preferred method to use for this work.

2.2.1 Proper Orthogonal Decomposition

The POD method finds a reduced basis by first creating a so-called snapshot matrix,

$$M = [y(\alpha_1), y(\alpha_2), ..., y(\alpha_p)]\,. \tag{2.8}$$

where the full order model is sampled p times at different parameter values. The vector containing the values of all the parameters can be called a parameter point, and the resulting output at a single parameter point is a snapshot. Then a singular value decomposition is performed on the snapshot matrix

$$M = U\Sigma V, \tag{2.9}$$

where Σ is a diagonal matrix with its entries being the singular values of M, and the columns of U and V are the left and right singular vectors, respectively [13]. The left singular vectors are the eigenvectors of the covariance matrix, defined as $C = MM^T$, and are chosen as the reduced basis. As the singular values are related to the importance of their corresponding vectors, choosing only the vectors with the largest singular values will give a minimal error when truncating the basis.

2.3 Perturbation theory

The solution of a system of equations is usually a field, which denotes the magnitude of a quantity of interest depending on the location in the domain. Typical examples of such quantities are temperature, or, in the application of this work, the neutron flux. Responses are values of interest that are estimated with the fields, and can be the maximum temperature, or the average of the field in a particular part of the domain. Commonly encountered responses in reactor physics are the multiplication factor, k_{eff}, and reaction rates.

The fields, and by extension the responses, are generally influenced by numerous variables such as the geometrical parameters, the material compositions and the nuclear data for each individual nuclide present in the system. During the design phase and further analysis, the variables may need to be changed numerous times to examine the behaviour of the model or the uncertainty in the input data. The changes to the variables will lead to perturbations in the fields, as well as perturbations to the responses.

Following the notation in [21], presume the system is defined by the equation of the form

$$AY = Q, \tag{2.10}$$

where A is the operator acting on the solution field Y, with Q the source term. All terms in the solution function shown in Equation (2.10) may depend on the variables of the model, which are again represented by the parameter vector α. The response can be defined by any response function $H(\alpha)$, such that

$$R = R[H(\alpha), Y(\alpha)]. \tag{2.11}$$

Equation (2.11) states that the response is a function of both the response function and the solution field. The response is also stated to depend explicitly on variables appearing in the response function and implicitly on variables appearing in the solution function.

We can set up the first order relation between a perturbed response and one variable by perturbing the variable and representing the perturbed response with a Taylor series expansion about the nominal unperturbed response value and discarding all higher order terms. Take the single unperturbed variable and the response as α_i^0 and R^0, and the perturbed ones to be α_i' and R', respectively, such that

$$R' \approx R^0 + \frac{\partial R}{\partial \alpha_i}\left(\alpha_i' - \alpha_i^0\right). \tag{2.12}$$

The relation holds if the perturbation is small enough or if the response depends nearly linearly on the variable. Commonly, Equation (2.12) is rewritten for relative changes, where S_{α_i} is introduced, which is the relative sensitivity coefficient of R with respect to α_i. The values of the perturbations themselves are written as ΔR and $\Delta\alpha_i$ for the response and variable, respectively, which gives

$$\begin{aligned} \Delta R &\approx \frac{\partial R}{\partial \alpha_i}\Delta\alpha_i \\ \frac{\Delta R}{R} &\approx S_{\alpha_i}\frac{\Delta\alpha_i}{\alpha_i}. \end{aligned} \tag{2.13}$$

Rewriting for the sensitivity coefficient gives:

$$\begin{aligned} S_{\alpha_i} &= \frac{\alpha_i}{R}\frac{\partial R}{\partial \alpha_i} \\ &\approx \frac{\Delta R/R}{\Delta\alpha_i/\alpha_i} \\ &\approx \frac{R' - R^0}{\alpha' - \alpha_i^0}\frac{\alpha_i}{R_0}. \end{aligned} \tag{2.14}$$

A new value of the response can be determined with the direct approach when combining Equation (2.13) and Equation (2.14):

$$\begin{aligned} R' &= R^0 + \frac{R}{\alpha_i}S_{\alpha_i} \\ &\approx R^0 + \frac{R' - R^0}{\alpha_i' - \alpha_i^0}. \end{aligned} \tag{2.15}$$

In this case, the system equations given in Equation (2.10) are solved for the nominal and perturbed value of the variable, and the response is determined for both solutions of $Y(\alpha)$. However, if the system is complex and costly to solve, the direct approach is not suitable for applications where many perturbations are required and for models with numerous variables.

A different approach can be used, which circumvents the recalculation of the solution field for each individual perturbation. For this method, the system is solved once at the nominal parameter values and once to determine the adjoint solution. Combining both solutions using general perturbation theory allows determining first order changes to the system without evaluating the system any further.

2.3.1 Adjoint Theory

To determine the adjoint of an operator, one starts from the definition of an adjoint:

$$\langle f, Ag\rangle = \langle A^* f, g\rangle, \tag{2.16}$$

where f and g are scalar functions in the domain of A and A^*, and A^* is the adjoint of the operator A [21]. The brackets indicate the inner product between the two terms inside them. In case of real functions and operators, and only the independent variable x, then

$$\langle f, Ag\rangle = \int_\Omega f(x)A(x)g(x)dx, \tag{2.17}$$

where the integral goes over the whole domain Ω. Using the definition from Equation (2.16), the adjoints of elementary operators, such as products or differentials, can be established. For linear operators, it becomes a straightforward task to determine the adjoint, as one just need to replace the elementary operators by their adjoint counterparts. In case of nonlinear operators, however, the procedure no longer consists of simply replacing the elementary operators and becomes more complicated.

Chapter 3

Methodology

In this chapter, the steps are given to retrieve the reduced models for the U-Battery. The ROMs are made with the solutions of the neutronics code for various models of the U-Battery. First, the details of these models are presented, which consists of a division into regions, a mesh to apply the FEM method, and a nuclear transport data library. Secondly, the neutronics solver PHANTOM-S_N is introduced. The solver outputs the neutron flux and the effective multiplication factor, and can also give other detector responses if defined. Lastly, the adaptive POD algorithm is explained. The POD code samples the outputs for varying parameter settings and computes the reduced model accordingly.

3.1 Models

Three models have been evaluated, where the geometry division, mesh, and energy resolution are varied. An overview of the parameters for the three models is given in Table 3.1. Due to the use of a discontinuous finite element method and hexagonal elements, there are 6 values for the flux output for each element. The complete flux solution is taken as a single column, such that its size becomes $n_{elements} \cdot n_{groups} \cdot 6$.

The first two models have two regions in their geometry, consisting of a single homogenized reflector and fuel region to lower the computational cost. A nuclide has been assigned to each region, with cross section data for each energy group. For the third model, however, the geometry is much more detailed and all the individual fuel blocks have their own region. Figure 3.1 shows the layout for the regions for a single axial layer, which is composed of 37 blocks. Due to symmetry, some regions have been given identical cross sections. These regions are illustrated with the different colours. With fewer unique nuclides, the number of possible variables is also reduced. The geometry of model three consists of a total of 151 regions, with 148 inner fuel regions for all fuel blocks divided over 4 layers, and three outer reflector regions for the top, bottom, and side reflectors. Furthermore, the mesh of the first two models has a total number of elements of 6912, while the third model has 6048 elements.

The first, second, and third model have 2, 6, and 17 energy groups respectively, with the upper bounds for each group given in Table 3.2. The table also gives the distribution of the flux across the groups, which indicates how much of the total flux inside the core resides in each group.

Table 3.1: Properties of the numerical models.

Model	Energy groups	Fuel regions	Reflector regions	Elements	Flux size
1	2	1	1	6912	82 944
2	6	1	1	6912	248 832
3	17	148	3	6048	616 896

Table 3.2: Upper energy bound for each group, and the distribution of the flux across the groups, given for the three models with 2, 6, and 17 energy groups, respectively.

Energy group	Upper bound [eV]			Distribution [%]		
	1	2	3	1	2	3
1	1.96×10^{7}	1.96×10^{7}	1.00×10^{8}	63.1	15.2	0.7
2	6.25×10^{-1}	1.83×10^{5}	3.68×10^{6}	36.9	36.6	15.0
3		1.20×10^{3}	1.11×10^{5}		6.1	7.3
4		1.55×10^{2}	1.66×10^{4}		6.6	5.9
5		1.76×10^{1}	3.35×10^{3}		22.2	5.5
6		2.38×10^{0}	7.49×10^{2}		13.2	6.0
7			1.37×10^{2}			5.3
8			2.76×10^{1}			2.2
9			1.37×10^{1}			2.9
10			5.04×10^{0}			2.1
11			2.36×10^{0}			4.1
12			6.25×10^{-1}			3.7
13			3.50×10^{-1}			10.0
14			1.89×10^{-1}			10.9
15			1.15×10^{-1}			12.7
16			5.00×10^{-2}			4.6
17			2.00×10^{-2}			1.2

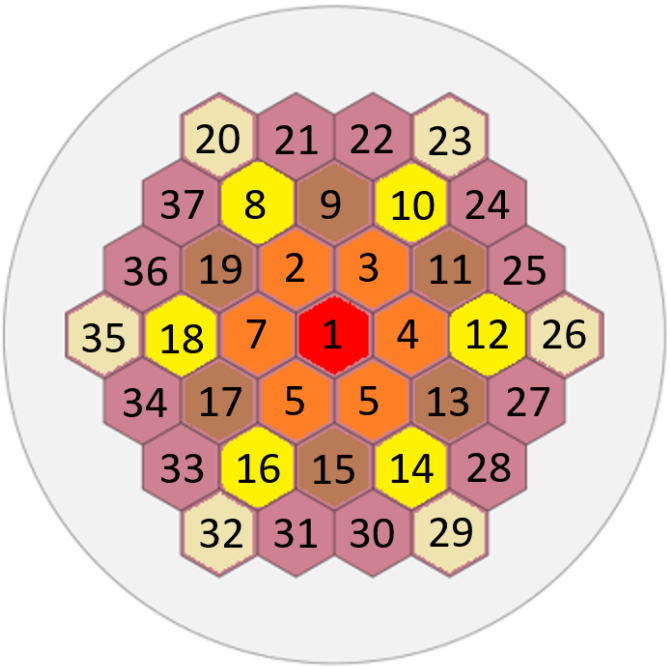

Figure 3.1: Layout of the fuel blocks for a single axial layer, with colours indicating the regions that have the same nuclear data due to symmetry (adapted from [14]).

Table 3.3: Parameters considered for model one with their nominal values. All capture and total scatter cross sections for the reflector region (2000), and also all fission cross sections for the fuel region (1000).

Parameter	Nominal value $[cm^{-1}]$	Parameter	Nominal value $[cm^{-1}]$
$\Sigma_{c,1}^{2000}$	1.56×10^{-5}	$\Sigma_{f,2}^{1000}$	6.84×10^{-3}
$\Sigma_{c,2}^{2000}$	2.00×10^{-4}	$\Sigma_{c,1}^{1000}$	1.14×10^{-3}
$\Sigma_{s,1}^{2000}$	4.41×10^{-1}	$\Sigma_{c,2}^{1000}$	1.68×10^{-3}
$\Sigma_{s,2}^{2000}$	4.87×10^{-1}	$\Sigma_{s,1}^{1000}$	3.43×10^{-1}
$\Sigma_{f,1}^{1000}$	4.15×10^{-4}	$\Sigma_{s,2}^{1000}$	3.96×10^{-1}

Table 3.4: Parameters considered for model two with their nominal values. All capture and total scatter cross sections for the reflector region (2000), and also all fission cross sections for the fuel region (1000).

Parameter	Nominal value $[cm^{-1}]$	Parameter	Nominal value $[cm^{-1}]$
$\Sigma_{c,1}^{2000}$	2.37×10^{-5}	$\Sigma_{f,4}^{1000}$	1.67×10^{-3}
$\Sigma_{c,2}^{2000}$	3.57×10^{-6}	$\Sigma_{f,5}^{1000}$	5.49×10^{-3}
$\Sigma_{c,3}^{2000}$	2.60×10^{-5}	$\Sigma_{f,6}^{1000}$	1.09×10^{-2}
$\Sigma_{c,4}^{2000}$	6.96×10^{-5}	$\Sigma_{c,1}^{1000}$	5.48×10^{-5}
$\Sigma_{c,5}^{2000}$	1.46×10^{-4}	$\Sigma_{c,2}^{1000}$	1.19×10^{-3}
$\Sigma_{c,6}^{2000}$	2.87×10^{-4}	$\Sigma_{c,3}^{1000}$	4.44×10^{-3}
$\Sigma_{s,1}^{2000}$	2.90×10^{-1}	$\Sigma_{c,4}^{1000}$	5.01×10^{-4}
$\Sigma_{s,2}^{2000}$	4.69×10^{-1}	$\Sigma_{c,5}^{1000}$	1.45×10^{-3}
$\Sigma_{s,3}^{2000}$	4.75×10^{-1}	$\Sigma_{c,6}^{1000}$	2.49×10^{-3}
$\Sigma_{s,4}^{2000}$	4.76×10^{-1}	$\Sigma_{s,1}^{1000}$	2.32×10^{-1}
$\Sigma_{s,5}^{2000}$	4.80×10^{-1}	$\Sigma_{s,2}^{1000}$	3.81×10^{-1}
$\Sigma_{s,6}^{2000}$	5.00×10^{-1}	$\Sigma_{s,3}^{1000}$	3.86×10^{-1}
$\Sigma_{f,1}^{1000}$	7.99×10^{-5}	$\Sigma_{s,4}^{1000}$	3.87×10^{-1}
$\Sigma_{f,2}^{1000}$	3.73×10^{-4}	$\Sigma_{s,5}^{1000}$	3.91×10^{-1}
$\Sigma_{f,3}^{1000}$	1.03×10^{-3}	$\Sigma_{s,6}^{1000}$	4.08×10^{-1}

The variables, or parameters, that are part of the models, are the nuclear data of each nuclide in the different regions. Only the transport data is used as parameters, more specifically the scatter, fission, and capture cross sections. The values in the library are determined via the continuous-energy Monte Carlo method with the use of Serpent [22]. For each region, the homogenized resonance shielded group cross sections are calculated at a constant temperature throughout the core. The parameters that are considered for each the first, second and third model are summarized in Table 3.3, 3.4 and A1, respectively.

The first model has been used to validate the usage of the applied ROM technique for the U-battery model, and to view its efficiency with regard to an increase of parameters. The second model could show this efficiency even better, as there are more variables. Additionally, the GPT module of PHANTOM-S_N has been verified on the second model. Lastly, the third model was to show the full capability of the ROM and GPT code on a much more detailed model, as well as to include the fission reaction-rate as an extra response besides the k_{eff} and the scalar flux. The additional detector response for model 3 determines the ratio of the fission reaction rate of a center region in one of the center layers to the total fission reaction rate across the reactor core. The response $R_{fission}$ is given by

$$R_{fission} = \frac{\int_E \int_{center} \Sigma_f(E)\phi(x,E)\ dxdE}{\int_E \int_{all} \Sigma_f(x,E)\phi(x,E)\ dxdE} \tag{3.1}$$

3.2 PHANTOM-S_N

The neutronic solver is the neutron transport code PHANTOM-S_N, a Delft University of Technology in-house code. It solves the multi-group transport equation, either in steady-state or time-dependent form, and has additional capabilities such as regular and generalized perturbation analysis [23]. The space discretization of the transport equation is done by the discontinuous Galerkin finite element method (DG-FEM) [24].

In this work, PHANTOM-S_N determines the multiplication factor and flux distributions of the U-Battery at steady state, which are fed as black-box outputs to the ROM code. Due to the discontinuous method and hexagonal elements of the mesh, the flux distribution consists of 6 values for each element. As the size of the output vector for the flux is determined by the number of energy groups, elements, and values per elements, the sizes are 82 944, 248 832 and 616 896, for the first, second and third model, respectively.

Besides solving the forward eigenvalue problems, the code can be set to solve both the forward and adjoint of the given systems and use generalized perturbation theory to compute the sensitivities of the multiplication factor and any other response to the nuclear data. It determines the change in the output for a 1% positive perturbation to the scatter, fission, or capture cross sections. For the group to group scatter cross sections, multiple values are perturbed simultaneously, as the sensitivities to the scatter cross sections to each group are not considered individually.

3.3 Adaptive POD algorithm

To retrieve a reduced model of the neutronics of the U-Battery, a nonintrusive adaptive POD code is used, given in detail in [25]. The code samples the solver outlined in Section 3.2 for different parameter settings, filling a snapshot matrix with the outputs. The algorithm uses an adaptive sampling strategy to minimize oversampling, while remaining capable of detecting regions of importance in the parameter space. The resulting ROM can therefore efficiently be determined and still be an accurate substitute for the high-fidelity neutronics solver.

The code builds a Smolyak interpolant for the coefficient $c_i(\alpha)$ in Equation (2.7) by considering the operator $U^i(c)(x)$ that approximating the coefficient with an expansion:

$$c(x) \approx U^i(c)(x) = \sum_{x_j^i \in \chi^i} c(x_j^i) a_{x_j^i}^i(x) \ , \tag{3.2}$$

where i is the level index, χ^i is the set of nodes x_j^i at level i, $a_{x_j^i}^i(x)$ are basis functions, and $c(x_j^i)$ is the function value at the support nodes x_j^i. Piecewise linear basis functions are considered, defined as follows [26]:

$$\begin{aligned} a_{x^1}^1 &= 1 \quad \text{if } i = 1 \ , \\ a_{x_j^i(x)}^i &= \begin{cases} 1 - (m^i - 1) \cdot |x - x_j^i|, & \text{if } |x - x_j^i| < \frac{1}{m^i - 1} \ , \\ 0, & \text{otherwise} \ , \end{cases} \end{aligned} \tag{3.3}$$

where m^i and the nodes x_j^i are defined as:

$$m^i = \begin{cases} 1 & \text{if } i = 1 \ , \\ 2^{i-1} + 1 & \text{if } i > 1 \ , \end{cases} \tag{3.4}$$

$$x_j^i = \begin{cases} 0.5 & \text{for } j = 1 \quad \text{if } m^i = 1 \ , \\ \frac{j-1}{m^i - 1} & \text{for } j = 1, 2, \ldots, m^i \quad \text{if } m^i > 1 \ . \end{cases} \tag{3.5}$$

Chapter 4

Results

4.1 Model 1: 2 groups

The two group model has a total of 10 possible variables in the nuclear data library, which are all used to build the reduced model. Their nominal values are detailed in Table 3.3. A single evaluation for the first model takes approximately 10 minutes with a single CPU core on a Linux cluster.

4.1.1 POD Modes

After the POD code has sampled enough points in the parameter space, the final POD modes are calculated. In Figure 4.1, the first three modes for the flux are shown for both energy groups. All modes highlight the symmetry of the design, especially mode one of the first group, with a smooth gradient of the fast neutron flux from the center to the outer region. While it is difficult to extract information visually from the second and higher modes due to their intricate shapes, the first modes can be used to gain insight in the flux distribution. One note on the modes, however, is their reversed sign, as can be seen at the colour bar. While the scalar flux itself is always positive, the POD modes are allowed to be negative. As the corresponding coefficient can be negative as well, the resulting solution will still be positive. Therefore, the magnitude is most important when looking at the POD modes.

It can readily be seen that the fast neutrons of group one are mainly present in the center region, where the fuel elements are the furthest away from the reflector that slows down the neutrons and where the majority of new neutrons are created, which are born in the high energy group. Furthermore, the mode for group two shows how the majority of the slow neutrons reside in the reflector, where moderation of the neutrons is the strongest. A noticeable contribution is present in the center as well, which stems from the high group one flux present in that area.

4.1.2 Validation

With the ROM at hand, it can be tested against the high-fidelity model. The error distribution between the two is plotted for 1000 random test points in Figure 4.2 for both the k_{eff} and the flux. Evaluating the test points with the reduced model takes less than a second on a personal computer. The vertical line denotes the POD termination tolerance that the algorithm aims for. For the k_{eff} , the maximum relative error is 4.68×10^{-4} and the mean relative error is 1.52×10^{-4}, while for the flux, the maximum and mean relative errors are 9.62×10^{-3} and 2.14×10^{-3}, respectively. All the errors are below the threshold, indicating that the reduced models have successfully been built.

4.1.3 Uncertainty Quantification

With the ROMs at hand, large numbers of evaluations can readily be computed. For both the k_{eff} and the maximum flux value of all groups, 100 000 Latin Hypercube samples are evaluated and the resulting density distributions are shown in Figure 4.3. The mean and standard deviations for both distributions are 1.338 ± 0.035 $[-]$ and 0.0511 ± 0.0017 $[cm^{-2}s^{-1}]$ for the k_{eff} and the maximum flux, respectively. The histograms approximate the Probability Distribution Function (PDF) and show a distribution that closely follows a normal distribution. If the model is linear

with respect to the parameters, this normal distribution is expected, as a uniform distribution is assumed for all parameters and their influence on the output is summed.

4.1.4 Efficiency

For the two group model, reduced models have been built with different numbers of parameters to evaluate the efficiency of the adaptive sampling algorithm. In Figure 4.4, the average and maximum relative errors are given for 100 test points for each ROM. In addition, Table 4.1 lists the number of total evaluations, important points and POD modes for the k_{eff} and the flux for each reduced model. The figures show that the error increases, which is caused by the large increase in parameter space. Still, all errors do remain well below the threshold of 1×10^{-3}. The k_{eff} error for 10 parameters being lower again is likely due to this ROM being enriched with additional samples, seen by the increase of important points in the table.

Regarding the table, there is always only a single POD mode for the k_{eff} since the output is a single number. The total evaluations are equal for the two different outputs, suggesting that the same settings have been evaluated for both outputs. The number of important points varies, however, meaning that more or different points in the parameter space resulted in an error above the threshold for the flux, such that they had to be included in the POD calculation.

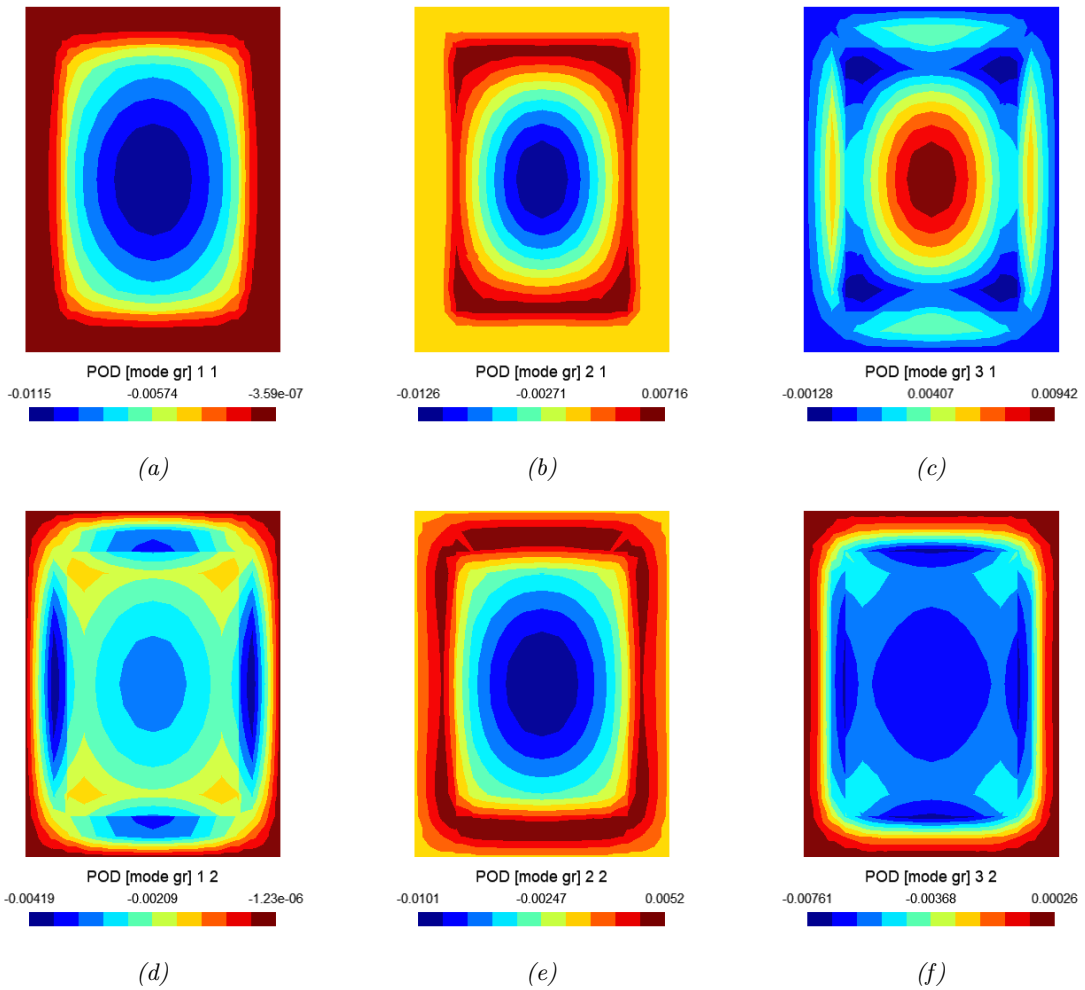

Figure 4.1: The first three POD modes for both energy groups of the 2 group model.

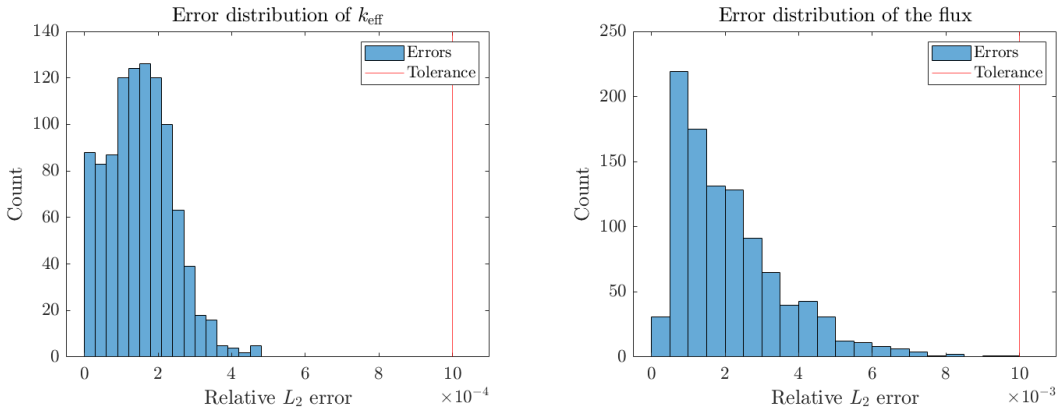

(a) *(b)*

Figure 4.2: Error distributions for 1000 test points with the set POD termination threshold in red of (a) the k_{eff} and (b) the flux.

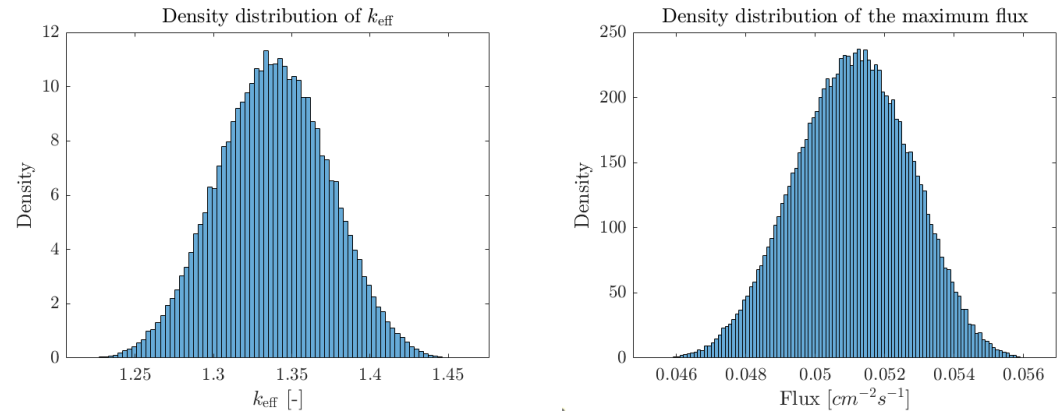

(a) *(b)*

Figure 4.3: Density distribution for 100,000 Latin Hypercube samples of (a) the k_{eff} and (b) the flux.

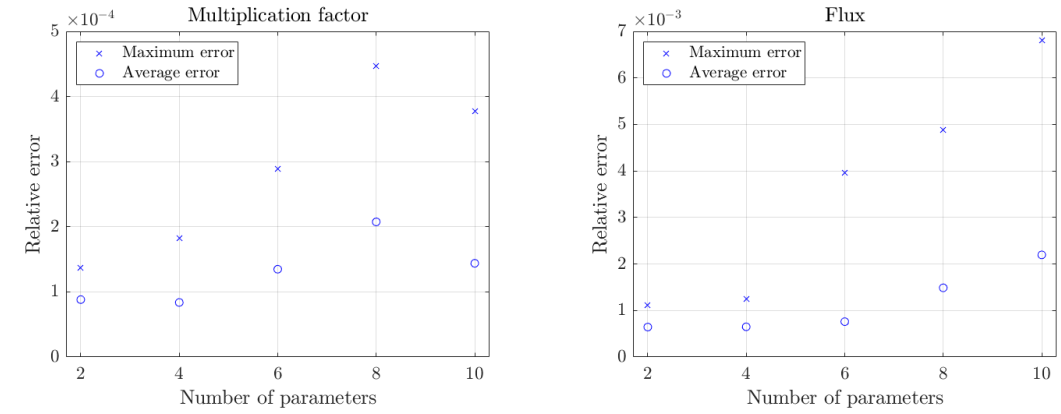

(a) *(b)*

Figure 4.4: Maximum and mean error of 100 test points for different numbers of parameters used in the ROM building for (a) the k_{eff} and (b) the flux.

Table 4.1: The number of evaluations, important points and POD modes for each ROM build with a different number of parameters for both the k_{eff} and the flux.

Number of parameters	Total evaluations		Important points		POD modes	
	k_{eff}	flux	k_{eff}	flux	k_{eff}	flux
2	13		9	9	1	9
4	27		11	15	1	13
6	63		30	42	1	30
8	115		56	74	1	39
10	183		95	99	1	43

Latin Hypercube samples have been calculated as well with the various reduced models for the model one, and the mean and standard deviation of the distributions are plotted as a function of the number of parameters in Figure 4.5. The figures show that an increase of the parameter space increases the standard deviation significantly for k_{eff}, while for the flux and both means the increase in parameters is less influential. The lack of change in uncertainty of k_{eff} from 2 to 4 parameters and large increase for going from 4 to 6 parameters, can be explained by which parameters are used for these models. The first two parameters are namely the scatter cross sections of the reflector region, and the next two parameters are the capture cross sections of the reflector. Other parameters are all cross sections of the fuel region, which appear to have a much larger influence on the k_{eff} , shown by Figure 4.5(a). Furthermore, the capture cross sections of the reflector region are relatively small values, such that a perturbation of these parameters is expected to be of minor importance to the k_{eff} , and therefore does not lead to a large increase in uncertainty. The same increase in uncertainty can be seen on a smaller scale for the flux.

The overall smaller variations in uncertainty for the flux are likely due to the particular response considered, which is a single value of the complete flux output. PHANTOM-S_N iterates till the total difference between flux vectors is below the given tolerance, and the POD code samples points till the error of the total flux vector between the high-fidelity model and the ROM is low enough. This leads to relatively large variations for single flux values, which causes larger relative uncertainties, regardless of the size of the parameter space, as can be seen in Figure 4.5(b).

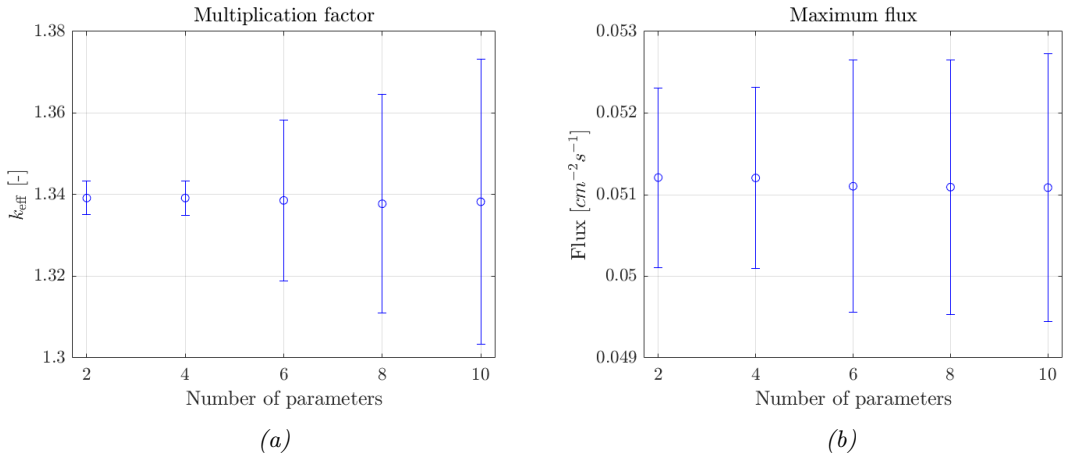

Figure 4.5: Mean and standard deviation of the 100,000 Latin Hypercube samples for different numbers of parameters used in the ROM building for (a) the k_{eff} and (b) the maximum flux.

4.2 Model 2: 6 groups

The six group model has additional transport data for each nuclide in the system, such that there are a total of 30 variables. The nominal values are given in Table 3.4. An evaluation on a single Linux cluster CPU now takes an 1 hour.

4.2.1 Validation

All variables have been used in the ROM building process, and 1000 test points have been evaluated to gauge the accuracy of the reduced model. Figure 4.6 presents the error distribution of the test points for the k_{eff} and the flux outputs. The maximum and mean relative errors are summarized in Table 4.2, and the number of evaluated points, important points and POD modes are detailed in Table 4.3. While not all test points are evaluated with the ROM with an accuracy below the threshold, there are only a few of such points. More precisely, there is only a single test point above the threshold for the k_{eff}, and 37 samples for the flux, meaning that 96% of the test points are in the acceptable error range for the flux output. Therefore, the reduced models are accepted as a successful surrogate for the high-fidelity model.

Importantly to note are the results of the ROM for the flux, which has also been built for a lower tolerance for selecting the important points of 1×10^{-3}. The results in Table 4.2 show that the selecting threshold has a large influence on the accuracy of the ROM. Additional points are sampled and enrich the ROM, but apparently they do not help with decreasing the errors for the test points. As this behaviour has not been observed for the ROMs of the k_{eff}, it may be caused by the large size of the flux vector and the relatively large variations in single flux values, which was already discussed in Section 4.1.4. These variations may behave as noise during the calculation of the POD modes, leading to modes used for the ROM which results in less accurate results.

4.2.2 Uncertainty Quantification

Instead of using the uniform Latin Hypercube samples to determine the distribution of k_{eff} and the maximum flux, we can assume that the uncertainties of the parameters follow a normal, or Gaussian, distribution. To see how this affect the density distributions of the responses, we can sample each parameter from a truncated Gaussian distribution rather than sampling the

Table 4.2: The maximum and mean of the errors of the 1000 testing points for each ROM build for model 3, which are the k_{eff} and two times the flux, with important points thresholds of $\epsilon_{high} = 5 \times 10^{-3}$ and $\epsilon_{low} = 1 \times 10^{-3}$ for the latter.

Quantity	k_{eff}	Flux_{high}	Flux_{low}
Maximum error	1.03×10^{-3}	1.30×10^{-2}	2.89×10^{-2}
Average error	3.33×10^{-4}	7.46×10^{-3}	8.50×10^{-3}

Table 4.3: The number of parameters, evaluations, important points and POD modes for each ROM build for model 2, which are the k_{eff} and two times the flux, with important points thresholds of $\epsilon_{high} = 5 \times 10^{-3}$ and $\epsilon_{low} = 1 \times 10^{-3}$ for the latter.

Quantity	k_{eff}	Flux_{high}	Flux_{low}
Number of parameters	30	30	30
Total evaluations	1413	542	1166
Important points	231	32	312
POD modes	1	32	111

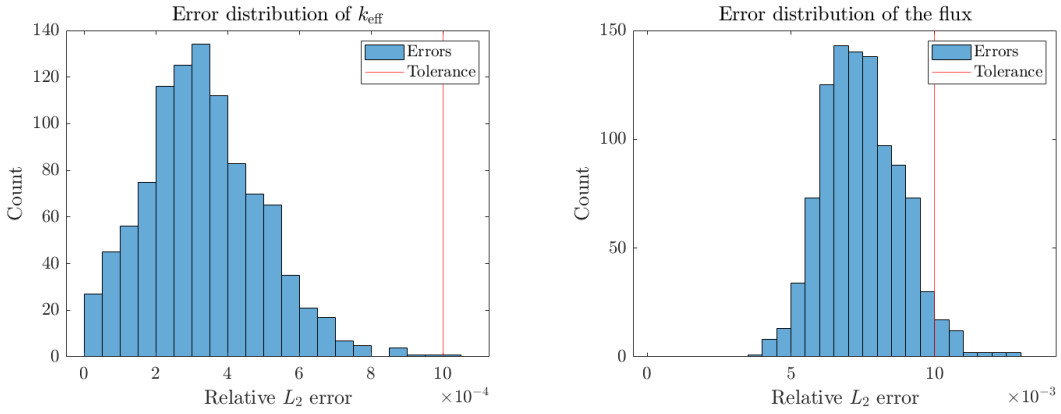

(a) *(b)*

Figure 4.6: Error distributions for 1000 test points with the set POD termination threshold in red of (a) the k_{eff} and (b) the flux.

parameters with the Latin Hypercube technique. In Figure 4.7(a), the distribution of 100 000 Gaussian samples is illustrated for a single parameter, where the following Gaussian function is used:

$$g(x) = \frac{1}{\sigma\sqrt{2\pi}} \exp\left\{-\frac{(x-\mu)^2}{2\sigma^2}\right\} \tag{4.1}$$

In Equation (4.1), $\mu = 0.5$ will be rescaled to the nominal value, and 0 and 1 to the values with a negative and positive perturbation of 10% of the nominal parameter value, respectively. The distributions are truncated at $\pm 2\sigma$, two standard deviations from the mean. This is done for consistency, to allow for easier comparison between the resulting density distributions of the responses, as the values that are sampled for the parameters will always be in the range that accounts for 95% of the Gaussian distribution. The distribution of the uniform Latin Hypercube samples with a range of $\pm 10\%$ are shown as well.

In Figures 4.7(b) and 4.7(c) the density distributions for the k_{eff} and the flux, respectively, are shown for samples taken from the truncated Gaussian distributions with different standard deviations. The distribution retrieved with the Latin Hypercube samples from Figure 4.7(a) is also plotted for comparison. The figures clearly show that reducing the spread in the parameter values reduces the spread in the response as well. Table 4.4 summarizes this observation as it details the standard deviations in the k_{eff} distribution for each Gaussian distribution from which the parameter values are sampled. In addition, the table gives the uncertainty of k_{eff} if the parameter values are sampled with the uniform Latin Hypercube technique instead, and for additional distributions with even smaller standard deviations.

Table 4.4: The standard deviations of the distributions of k_{eff} for varying standard deviations in the sampling distributions. The percentage of perturbation from the mean gives the range of the distributions. The average of the means of the distributions of k_{eff} is 1.3261.

Perturbation [%]		$\sigma_{samples}$ [-]		$\sigma_{k_{\text{eff}}}$ [-]		$\sigma_{k_{\text{eff}}}$ [pcm]	
LHS	Gaussian	LHS	Gaussian	LHS	Gaussian	LHS	Gaussian
10		0.2887	0.2500	0.0247	0.0187	1866	1413
5		0.1443	0.1250	0.0123	0.0093	932	703
2.5		0.0722	0.0625	0.0062	0.0046	466	346
1.25		0.0361	0.0312	0.0031	0.0023	233	175
0.625		0.0180	0.0156	0.0015	0.0012	117	87

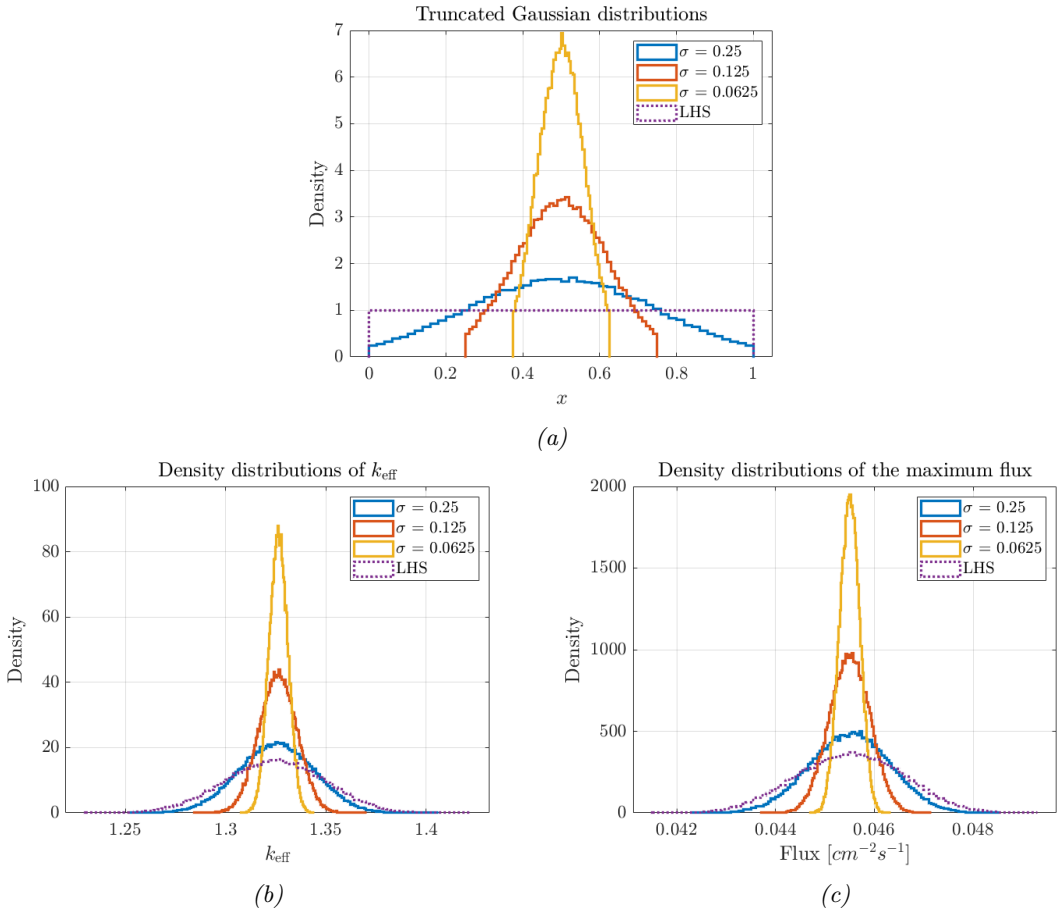

Figure 4.7: (a) Truncated distributions for 100,000 samples of the Gaussian function of Equation (4.1), and the density distributions calculated with the Gaussian samples of (b) the k_{eff} and (c) the maximum flux.

4.2.3 Sensitivities

For the six group model, the sensitivities of k_{eff} are determined with the GPT module of PHANTOM-S_N. All 30 variables have been perturbed individually, and the response perturbations have been calculated via the adjoint way. Figure 4.8 presents the sorted absolute sensitivities, while Table 4.5 details the numerical values and the corresponding region, reaction, and group of the variable.

The k_{eff} is influenced mainly by the occurrence of fission reactions, and the different neutron reactions either increase or decrease the number of possible fissions. Capture reactions take away neutrons from the system, such that they can no longer undergo a fission reaction, leading to a negative sensitivity. A higher fission probability clearly increases the number of fission reactions. Scatter reactions, however, have a more subtle influence, as they not only influence the movement of neutrons in space, but in energy level as well. This means that scatter reactions have an influence on the k_{eff} that is twofold. Scatter reactions can bounce neutrons back towards the center of the reactor core, where they have the highest probability to undergo fission. A scatter reaction can also downscatter a neutron to a lower energy group, where the fission probability becomes higher as well. The only exception to this is the scatter for the lowest energy group, as can be seen in Table 4.5 for group six of the fuel region. Its sensitivity is negative because neutrons can no longer downscatter to an even lower group with a higher probability for fission. This means that a positive perturbation of this scatter variable only increases the probability for a scatter reaction to occur, and the probability for a fission therefore decreases relative to the

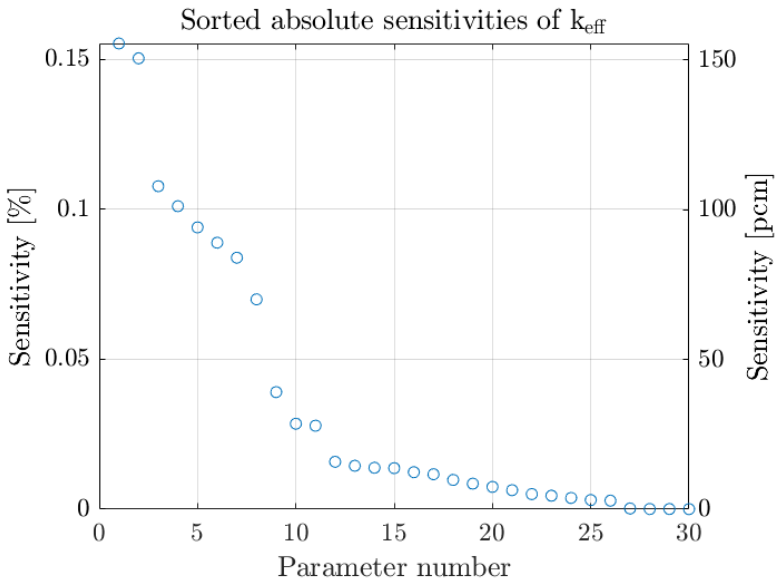

Figure 4.8: Sensitivities of k_{eff} to all parameters of the 6 group model in percentages and in pcm for a nominal k_{eff} of 1.3266.

unperturbed case, leading to a negative influence on the k_{eff}.

Figure 4.8 clearly shows that not all variables are important to the k_{eff}, and only eight of them have an influence above 0.05%, or 50 pcm at a nominal k_{eff} of 1.3266. It can be seen from the table that the most unimportant cross sections are all capture reactions from the reflector and a single capture of the fuel region, which is due to these variables having the lowest values of all nuclear data, as shown in Table 3.4. The same reasoning can not immediately be made for the most important variables, as their order is generally not tied to only the size of their values. Another influence on the sensitivity values is the size of the average neutron flux for each group. The distribution of the flux given in Table 3.2 indicates that most neutrons live in the second energy group, which, together with the size of the variables, explains why capture and scatter of group two have the highest sensitivities. The order of the next variables is a balance between their size and the size of the flux in the corresponding energy group of the variable.

Using the sensitivity values, a linear approximation of the response perturbation can be calculated for the Latin Hypercube samples. The comparison between the density distribution of k_{eff} determined with the ROM and with the GPT sensitivities is presented in Figure 4.9. The results indicate that the six group model is closely linear. For these cases, the GPT technique can efficiently retrieve sensitivities of all parameters, which can effectively be used as a reduced model as well.

To verify the linearity of the model, the number of unique nodes for each parameter are given by Table 4.6. The number is determined by the adaptive sampling algorithm and denotes the number of points sampled along each dimension. The parameter is considered constant for a value of 3, as the error was found to be within the tolerance at the two sample points at the maximum and minimum perturbation of the parameter value, and the algorithm stopped further sampling. A value of 5 indicates a linear dependency, while higher values indicate non-linearity along that dimension. The table shows that the POD algorithm found the model to be constant with respect to the four parameters with the lowest sensitivities, and that the k_{eff} has a linear dependency to all others.

Table 4.5: The sensitivity values for the six group model for a one-percent perturbation in the cross section data at a nominal k_{eff} of 1.3266. Region 1000 is the fuel part, region 2000 is the reflector, and group one is the fast group.

Parameter	Sensitivity [pcm]	Region	Reaction	Group
$\Sigma_{c,2}^{1000}$	−155	1000	capture	2
$\Sigma_{s,2}^{1000}$	150	1000	scatter	2
$\Sigma_{c,3}^{1000}$	−108	1000	capture	3
$\Sigma_{s,3}^{1000}$	101	1000	scatter	3
$\Sigma_{f,5}^{1000}$	94.0	1000	fission	5
$\Sigma_{f,6}^{1000}$	88.9	1000	fission	6
$\Sigma_{c,5}^{1000}$	−83.9	1000	capture	5
$\Sigma_{c,6}^{1000}$	−70.0	1000	capture	6
$\Sigma_{f,2}^{1000}$	39.1	1000	fission	2
$\Sigma_{s,1}^{1000}$	28.5	1000	scatter	1
$\Sigma_{s,2}^{2000}$	27.9	2000	scatter	2
$\Sigma_{s,5}^{2000}$	15.8	2000	scatter	5
$\Sigma_{s,1}^{2000}$	14.5	2000	scatter	1
$\Sigma_{f,4}^{1000}$	13.8	1000	fission	4
$\Sigma_{c,4}^{1000}$	−13.7	1000	capture	4
$\Sigma_{f,3}^{1000}$	12.4	1000	fission	3
$\Sigma_{s,6}^{1000}$	−11.7	1000	scatter	6
$\Sigma_{s,4}^{1000}$	9.78	1000	scatter	4
$\Sigma_{s,6}^{2000}$	8.54	2000	scatter	6
$\Sigma_{s,3}^{2000}$	7.45	2000	scatter	3
$\Sigma_{s,5}^{1000}$	6.36	1000	scatter	5
$\Sigma_{s,4}^{2000}$	5.05	2000	scatter	4
$\Sigma_{f,1}^{1000}$	4.51	1000	fission	1
$\Sigma_{c,6}^{2000}$	−3.77	2000	capture	6
$\Sigma_{c,1}^{1000}$	−3.06	1000	capture	1
$\Sigma_{c,5}^{2000}$	−2.86	2000	capture	5
$\Sigma_{c,4}^{2000}$	−0.240	2000	capture	4
$\Sigma_{c,3}^{2000}$	−0.0718	2000	capture	3
$\Sigma_{c,1}^{2000}$	−0.0715	2000	capture	1
$\Sigma_{c,2}^{2000}$	−0.0385	2000	capture	2

Table 4.6: Unique nodes for each parameter evaluated by the POD code, sorted by sensitivity value.

	Parameter	Unique nodes		Parameter	Unique nodes
1	$\Sigma_{c,2}^{1000}$	5	16	$\Sigma_{f,3}^{1000}$	5
2	$\Sigma_{s,2}^{1000}$	5	17	$\Sigma_{s,6}^{1000}$	5
3	$\Sigma_{c,3}^{1000}$	5	18	$\Sigma_{s,4}^{1000}$	5
4	$\Sigma_{s,3}^{1000}$	5	19	$\Sigma_{s,6}^{2000}$	5
5	$\Sigma_{f,5}^{1000}$	5	20	$\Sigma_{s,3}^{2000}$	5
6	$\Sigma_{f,6}^{1000}$	5	21	$\Sigma_{s,5}^{1000}$	5
7	$\Sigma_{c,5}^{1000}$	5	22	$\Sigma_{s,4}^{2000}$	5
8	$\Sigma_{c,6}^{1000}$	5	23	$\Sigma_{f,1}^{1000}$	5
9	$\Sigma_{f,2}^{1000}$	5	24	$\Sigma_{c,6}^{2000}$	5
10	$\Sigma_{s,1}^{1000}$	5	25	$\Sigma_{c,1}^{1000}$	5
11	$\Sigma_{s,2}^{2000}$	5	26	$\Sigma_{c,5}^{2000}$	5
12	$\Sigma_{s,5}^{2000}$	5	27	$\Sigma_{c,4}^{2000}$	3
13	$\Sigma_{s,1}^{2000}$	5	28	$\Sigma_{c,3}^{2000}$	3
14	$\Sigma_{f,4}^{1000}$	5	29	$\Sigma_{c,1}^{2000}$	3
15	$\Sigma_{c,4}^{1000}$	5	30	$\Sigma_{c,2}^{2000}$	3

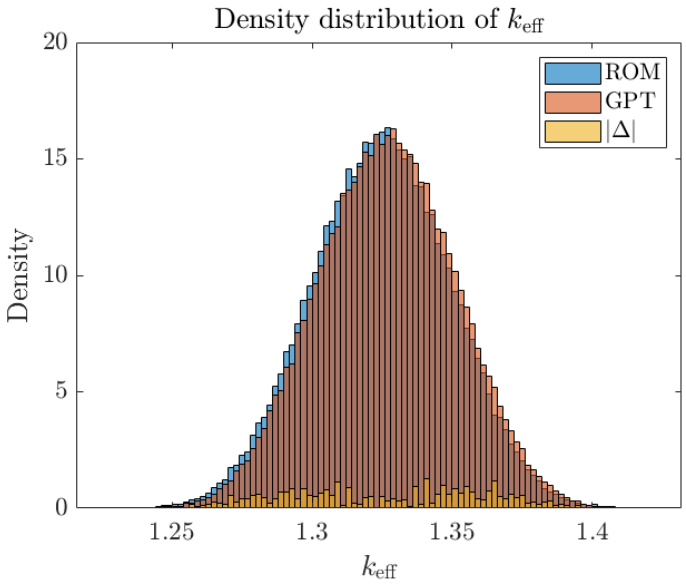

Figure 4.9: Density distribution of the 6 group model for 100,000 LHS for both the ROM and with the sensitivities of the GPT code, with the absolute difference shown for clarity.

4.3 Model 3: 17 groups

On top of the added energy groups, the 17 groups model also has more regions, leading to a total of 1122 variables. Building a reduced model with all the possible variables would be impractically costly. More importantly, it would be completely redundant, as not every parameter will have a noticeable influence on the output. As a solution, we use perturbation theory to choose a set of parameters. With the help of the GPT module of PHANTOM-S_N, the complete set of variables can be sorted by their influence on the output. We have chosen the 50 variables with the highest sensitivity values to be part of the ROM, which are discussed later. With a single Linux cluster CPU, an evaluation takes around 10 hours for the third model.

Apart from the k_{eff} and the flux output, for this model a ROM has been built for another output as well. Equation (3.1) gives the fission reaction rate ratio for one of the center regions, normalized by the total fission reaction rate across all regions. The ratio is an indication of the power peaking in the reactor, and the sensitivities enable one to see which cross sections can dampen the peak most significantly. The ROM for this output has been built for only the most important 20 variables, determined by the sensitivity values, but in this case with the sensitivities of the response given by Equation (3.1). Fewer variables were considered to lower the computational time, and because the POD code assumed the variables of the k_{eff} with the lowest sensitivities to be constant, which was expected to occur for this response as well.

4.3.1 Validation

The resulting ROMs have been tested with only 100 random points, due to the large time cost involved with solving the model. Figure 4.10 presents the error distribution for the k_{eff}, the flux and the additional response.

Almost half of the errors are above the threshold for the k_{eff}, 44 in total, while only a single error is too high for the flux. The maximum and mean errors are summarized in Table 4.7 for the three outputs. The main cause for this discrepancy between the error distributions of the ROMs are the tolerances set for the building phase. The termination and important points tolerances were 1×10^{-3} and 5×10^{-4} for the k_{eff}, and 1.5×10^{-2} and 5×10^{-3} for flux, respectively. These tolerance settings lead to relatively more sampled points taken into the POD calculation for the flux, while more points are discarded as unimportant for the k_{eff}, as presented by Table 4.8.

It is clear that the values of the POD tolerances largely determine the size of the average testing error, but the distribution of the errors must be taken into account as well. Figure 4.10(a) shows

Table 4.7: The maximum and mean of the errors of the 100 testing points for each ROM build for model 3, which are the k_{eff}, the flux, and the fission rate detector.

Quantity	k_{eff}	Flux	R_f
Maximum error	2.87×10^{-3}	1.60×10^{-2}	2.59×10^{-2}
Average error	9.17×10^{-4}	9.12×10^{-3}	7.98×10^{-3}

Table 4.8: The number of parameters, evaluations, important points and POD modes for each ROM build for model 3, which are the k_{eff}, the flux, and the fission rate detector.

Quantity	k_{eff}	Flux	R_f
Number of parameters	50	50	20
Total evaluations	525	101	59
Important points	30	40	7
POD modes	1	38	1

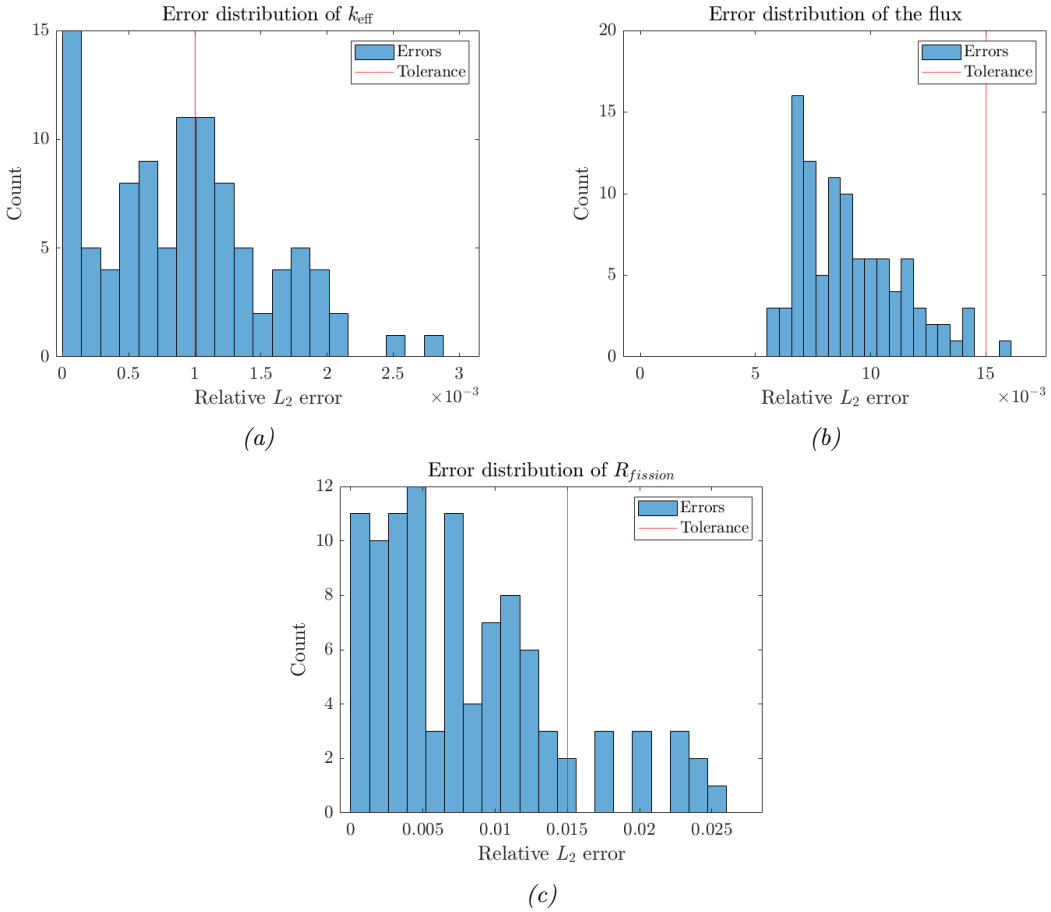

Figure 4.10: Error distributions for 100 test points with the set POD termination threshold in red of (a) the k_{eff}, (b) the flux and (c) the fission reaction rate ratio.

that the combination of important points and termination tolerances must be carefully chosen, to prevent the POD code from discarding too many points. The consequence could otherwise be a termination of the algorithm before a ROM is built that is actually accurate enough when testing it for the random evaluations. Including more points leads to a more enriched ROM that is expected to have more errors below the termination tolerance for the testing points.

4.3.2 Uncertainty Quantification

As with the second model, these ROMs have also been evaluated for 100 000 truncated Gaussian samples, and the resulting density distributions are presented in Figure 4.11. The distributions are determined with a set of samples with a uniform distribution retrieved with the Latin Hypercube technique with the largest range of ±10%, and for three truncated Gaussian distributions with varying uncertainty. See Figure 4.7(a) for the unscaled sample distributions.

The distributions for the flux and detector response have an equal mean for each of them, and narrower density distributions for those determined with narrower sample distributions. This suggests that the model is linear for these outputs, as the effect of the varying ranges of the parameter distributions is directly transferred through the model to the output, without deviating from the average.

The k_{eff}, however, shows a deviation from this trend, as the means of its distributions shift. The most likely explanation for this is an inadequate ROM. As discussed, the error distributions of the tested points show that it is relatively less accurate than the other ROMs. If this inaccuracy

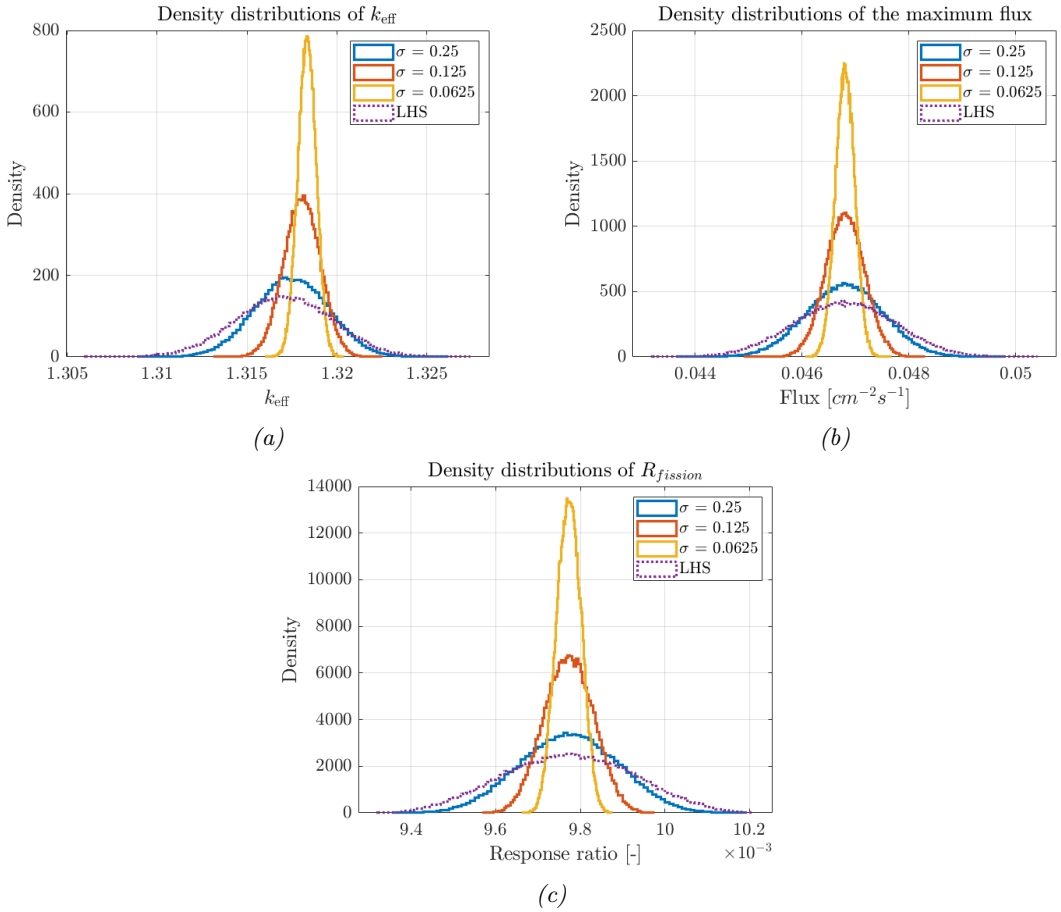

Figure 4.11: Density distributions for 100 000 *truncated Gaussian samples and the LHS samples with the largest variance (see Table 4.4) of (a) the k_{eff}, (b) the flux and (c) the fission reaction rate ratio.*

is present only for a specific part of the parameter space, the part leading to higher k_{eff} values, it can explain the distributions of Figure 4.11(a), where the means are displaced from each other. In Table 4.9, the number of unique nodes for the parameters with the highest sensitivities is given, including their location. The values show that certain variables have four nodes, which means they are not sampled further in one part of their dimension. For parameter values in this unsampled part, the k_{eff} is assumed constant with respect to these parameters. The constant value is taken as the nominal value, as the POD algorithm determined that this value already evaluates the k_{eff} accurately enough in the unsampled region. All parameters with a partly unsampled region have a positive influence on the k_{eff}, such that the ROM is indeed expected to give consistently lower values for the k_{eff} for a part of the parameter space.

The k_{eff} has also been evaluated with the GPT sensitivities for the 100 000 truncated Gaussian samples with an uncertainty of $\sigma = 0.0625$. The comparison between the ROM and the linear approximation is illustrated in Figure 4.12, which again shows a consistently lower evaluation for the k_{eff} by the ROM. As the ROM has been determined to contain an intrinsic bias towards lower k_{eff}, the results of the figure cannot be used to assess the linearity of the third model.

4.3.3 Sensitivities

Sensitivities to all the 1122 possible variables have been computed with the GPT module for both the k_{eff} and the fission rate detector. The highest 50 for the k_{eff} and 20 for the detector have been considered for the ROM and are summarized in Table A2 and A4, respectively. The top

Table 4.9: Unique nodes for the top twelve parameters with the highest sensitivities, evaluated by the POD code for the k_{eff} of model 3, sorted by sensitivity value. The location of the nodes on each dimension is also given

	Parameter	Unique nodes	Location
1	$\Sigma_{s,2}^{1100}$	5	(0, 0.25, 0.5, 0.75, 1)
2	$\Sigma_{s,15}^{1100}$	4	(0, 0.25, 0.5, 1)
3	$\Sigma_{s,14}^{1100}$	4	(0, 0.25, 0.5, 1)
4	$\Sigma_{s,13}^{1100}$	4	(0, 0.25, 0.5, 1)
5	$\Sigma_{s,7}^{1100}$	4	(0, 0.25, 0.5, 1)
6	$\Sigma_{s,6}^{1100}$	4	(0, 0.25, 0.5, 1)
7	$\Sigma_{s,3}^{1100}$	3	(0, 0.5, 1)
8	$\Sigma_{s,5}^{1100}$	3	(0, 0.5, 1)
9	$\Sigma_{s,4}^{1100}$	3	(0, 0.5, 1)
10	$\Sigma_{s,9}^{1100}$	3	(0, 0.5, 1)
11	$\Sigma_{s,8}^{1100}$	3	(0, 0.5, 1)
12	$\Sigma_{s,11}^{1100}$	3	(0, 0.5, 1)

12 sensitivities are also presented separately in Table 4.10 for the k_{eff} and in Table 4.11 for the detector, as these are the most important for the outputs. Figures 4.13 and 4.14 show the sorted absolute sensitivities for respectively the k_{eff} and the detector. The figures clearly indicate that discarding many of the possible parameters is indeed a valid approach, as only a select group of the parameters will have a significant influence on the outputs. The particular variables showing up in the tables and their order are further discussed in Section 5.2.

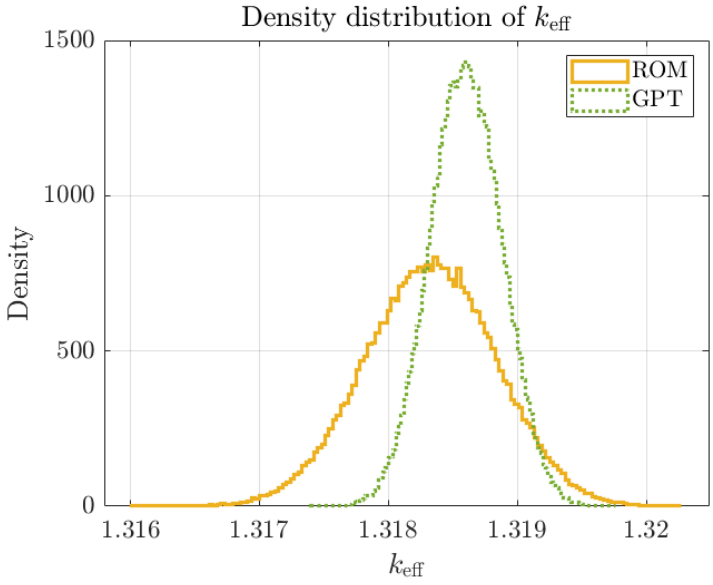

Figure 4.12: Density distribution of the k_{eff} for 100 000 truncated Gaussian samples with an uncertainty of $\sigma = 0.0625$, computed with the ROM and the GPT sensitivities.

Table 4.10: The top twelve sensitivity values of the k_{eff} for the 17 group model for a one-percent perturbation in the cross section data at a nominal k_{eff} of 1.3186. Region 1100 is the side reflector region, and group one is the fast group.

Parameter	Sensitivity [pcm]	Region	Reaction	Group
$\Sigma_{s,2}^{1100}$	11.2	1100	scatter	2
$\Sigma_{s,15}^{1100}$	5.39	1100	scatter	15
$\Sigma_{s,14}^{1100}$	5.07	1100	scatter	14
$\Sigma_{s,13}^{1100}$	4.97	1100	scatter	13
$\Sigma_{s,7}^{1100}$	4.88	1100	scatter	7
$\Sigma_{s,6}^{1100}$	4.37	1100	scatter	6
$\Sigma_{s,3}^{1100}$	4.03	1100	scatter	3
$\Sigma_{s,5}^{1100}$	3.49	1100	scatter	5
$\Sigma_{s,4}^{1100}$	3.47	1100	scatter	4
$\Sigma_{s,9}^{1100}$	3.33	1100	scatter	9
$\Sigma_{s,8}^{1100}$	2.73	1100	scatter	8
$\Sigma_{s,11}^{1100}$	2.62	1100	scatter	11

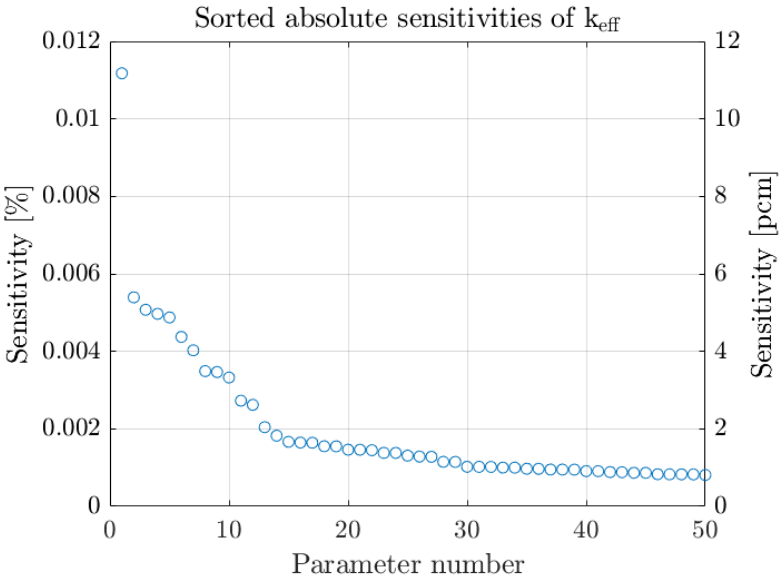

Figure 4.13: Sensitivities of k_{eff} to all parameters of the 17 group model.

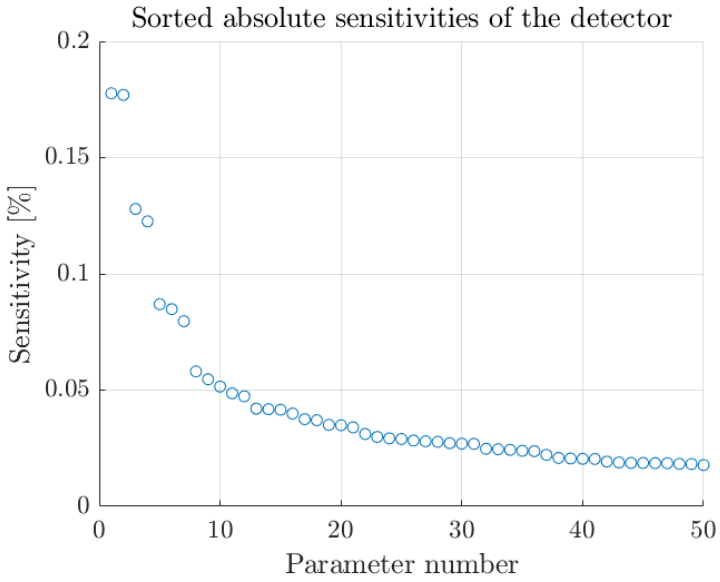

Figure 4.14: Sensitivities of the detector response to the top 50 parameters of the 17 group model, with the detector being the fission reaction rate of one of the center regions divided by the total fission reaction rate.

Table 4.11: The top twelve sensitivity values of the fission reaction rate detector response for the 17 group model for a one-percent perturbation in the cross section data at a nominal response value of 9.77×10^{-3}*. Region 1100 and 1401 are the side and top reflector, respectively, region 2201 is the center fuel region considered in Equation (3.1), and group one is the fast group.*

Parameter	Sensitivity [%]	Region	Reaction	Group
$\Sigma_{s,13}^{1100}$	1.78×10^{-1}	1100	scatter	13
$\Sigma_{f,15}^{2201}$	1.77×10^{-1}	2201	fission	15
$\Sigma_{f,13}^{2201}$	1.28×10^{-1}	2201	fission	13
$\Sigma_{f,14}^{2201}$	1.23×10^{-1}	2201	fission	14
$\Sigma_{f,16}^{2201}$	8.70×10^{-2}	2201	fission	16
$\Sigma_{s,15}^{1100}$	8.48×10^{-2}	1100	scatter	15
$\Sigma_{s,14}^{1100}$	7.96×10^{-2}	1100	scatter	14
$\Sigma_{s,12}^{1100}$	5.80×10^{-2}	1100	scatter	12
$\Sigma_{s,2}^{2201}$	5.47×10^{-2}	2201	scatter	2
$\Sigma_{s,13}^{1401}$	5.15×10^{-2}	1401	scatter	13
$\Sigma_{s,11}^{2101}$	4.86×10^{-2}	2201	scatter	11
$\Sigma_{s,2}^{1401}$	4.73×10^{-2}	1401	scatter	2

Chapter 5

Discussion

5.1 Efficiency

The accuracy of the ROM is quantified by the test points and the resulting number of errors below the threshold. Clearly, the accuracy is sensitive to the POD tolerances, such that lowering the termination tolerance leads to smaller errors. Lower tolerances simultaneously require more samples for the algorithm to terminate. If computational time is not abundantly available, a delicate balance must be found between the cost and the quality of the ROM. The exact relation between the two is, however, not known beforehand. An easily applicable remedy may be to start with a large tolerance, and keep lowering it until the ROM produces errors of an acceptable size. Each time the POD code runs again, it starts with sampling the same parameter settings until the previous tolerance threshold has been crossed and additional points are sampled to enrich the ROM. These initial evaluations would not need to run again, as the solutions can be saved and reread by the POD code, such that no computational effort is wasted.

In addition, the threshold for selecting important points may not always need to be exactly one magnitude lower than the termination tolerance. As noted in Section 4.2.1 for the flux output, it has been found that setting a larger tolerance for the important points actually decreased the maximum error between the high-fidelity model and the ROM for the test points. The selection tolerance was taken as half of the termination tolerance, and should always remain below the latter to prevent oversampling or non-termination. An explanation for this behavior has been suggested to be the large size of the flux vector and the large relative variations between individual flux values. It can be that additional points added to the snapshot matrix at some point lead to noise in the POD mode, which in turn reduces the accuracy of the ROM for points outside the sampling set.

A straightforward solution seems to be to not set the selecting tolerance too far from the termination tolerance. However, as commented in Section 4.3.1, this can lead to the exact same problem for other responses such as the k_{eff}. The higher selecting tolerance resulted in this case in fewer sample points being included in the snapshot matrix. The resulting ROM for k_{eff} had high errors for the testing points, which is likely due to a lack of enrichment, as shown by the results of Table 4.8. Consequently, for every response it will be needed to find a balance between the termination and important points selecting tolerances, both to limit oversampling and to ensure that the ROM remains accurate.

In regard to computational cost, the ROM heavily reduces the time required for evaluations. Even for the ROMs of model 3, which comes with the highest number of parameters and largest flux vector, evaluating 100 000 samples takes approximately one second on a personal computer. For comparison, a single full model evaluation takes around 10 hours to complete. The gain in computation time for these ROMs is a factor of about 1×10^7, displaying the advantages of using reduced order models, even in the case of a large upfront cost.

5.2 Sensitivities

For model 2, the order of the parameters has been discussed in Section 4.2.3. The conclusion was that the order is determined by the size of the nominal values of the parameters and the size of the flux in the corresponding energy group of the parameter. A third influence on the order of the parameters is revealed by the GPT results for the third model, laid out in Table 4.10 and 4.11 for the twelve most important parameters for respectively the k_{eff} and the fission reaction rate ratio detector. The additional influential quantity is the size of the region corresponding to the variable. While the results for model 2 in Table 4.5 predominantly show parameters of the fuel region, this is the opposite for the results for model 3, where only reflector parameters show up. The only differences between the two models are the division into finer energy groups and smaller regions for model 3. The effect of the fine groups is assumed to be of the same magnitude on both reflector and fuel regions. The ratio of volumes for fuel and reflector regions, however, changes considerably, as the side reflector is still relatively large compared to the individual fuel regions. The deduction of the third influence is reinforced by looking at the magnitudes of the sensitivities, which is lower for all parameters. This is expected considering that the perturbations of the parameters actually changes the properties of a smaller part of the reactor core for model 3, and the resulting influence on the responses would then indeed be less.

It is therefore recommended to either normalize the computed sensitivities by the volume of the region, or sum up the reactions per group for the fuel and reflector part of the geometry. Summing the sensitivities to go back to a single fuel and reflector region is a valid strategy, as the values are linearly approximated. It enables one to view the influence of perturbing properties of all fuel blocks or the whole reflector simultaneously. This can be useful in the design phase, as the fuel blocks are initially chosen to have identical layout and material properties. The summed sensitivities then give an indication of the influence of modifying these properties.

Normalizing to the volume gives the sensitivities of the parameters per cm^3 of nuclide material in the corresponding region, which allows for easier comparison between the parameters regardless of the size of their region. This is especially helpful in case there are local changes, for example due to a partial coolant channel blockage or higher burnup in the center of the core. Such a change can be modeled as a perturbation in the nuclear data, and the sensitivities of individual parameters can then directly give an indication for their influences on the responses.

Chapter 6

Conclusion

Due to the rising demand for non-carbon energy production and the limitations of renewable methods such as solar and wind energy, interest in nuclear reactors have started to regrow. Small modular reactors (SMRs) suffer less from the limitations of large nuclear plants, and thus are a promising alternative to use as a replacement for fossil-fueled energy production. The U-Battery is one example of an SMR and the particular design considered in this work. To ensure safe use of the design during all operating conditions and throughout its whole lifetime, high-fidelity numerical models are made to reflect reality as accurately as possible. However, the computational cost for these models becomes unmanageable for many-query applications such as uncertainty quantification. In this work, a method is presented to alleviate the demand for computational resources by applying a nonintrusive adaptive proper orthogonal decomposition algorithm in combination with perturbation theory. Furthermore, the method is applied on three different neutronics models of the U-Battery, varying in complexity, to analyze the performance of the method.

The reduced order modeling technique considered in this work is proper orthogonal decomposition (POD), combined with an adaptive sampling strategy. Three different high-fidelity models for the neutronics of the U-Battery have been reduced, which vary in energy group resolution and number of regions in the geometry. The first and second model had a geometry with only two regions, one for the reflector and one for the fuel part of the core, and the geometry of the third model contained separate regions for all fuel blocks and three regions for the reflector. The first, second and third model had a number of energy groups of respectively 2, 6 and 17. The reduced models have been built for two responses, the k_{eff} and the full flux vector. The results for the first model show that an increase in parameter space decreases the accuracy of the reduced order model (ROM) and increases the uncertainty of the responses.

To limit the number of parameters considered in the ROM building, general perturbation theory (GPT) has been applied to determine the sensitivities of the response to all the parameters. This showed for the second model that not all parameters were equally important, such that those with low sensitivities could be assumed constant. A comparison between the results of the GPT module in PHANTOM-S_N and the ROM for k_{eff} in Figure 4.9 indicates that the second model is closely linear, which is also confirmed by the number of unique nodes gathered by the POD code, shown in Table 4.6.

For the third model, it has been demonstrated that the POD tolerances heavily impact the accuracy of the ROM. The termination tolerances must be carefully considered, to balance the computational cost of the building phase with the resulting accuracy of the ROM. Depending on the response considered, the important points threshold tolerance can cause too many points to be discarded, leading to a ROM that lacks enrichment of the parameter space. The ROM of the k_{eff} for the third model was determined to be built with such inadequate POD tolerances, which lead to only part of the parameter space being undersampled and resulting in a reduced model with a bias towards lower k_{eff}.

The important points threshold can also cause oversampling, such as for the flux vector output. In this case, the POD code includes too many points in the snapshot matrix, because the individual flux values already contain a large uncertainty. This occurrence is however more of a limitation of the high-fidelity model, which is the initial source of this uncertainty.

The sensitivities to all parameters of the third model have been computed, and the top 50 are summarized in Table A2. The quantities that affect the order of the parameters have been determined to be the magnitude of their nominal values, the portion of the total flux residing in the corresponding energy group of the parameter, and the volume of the region corresponding to the parameter. Due to not considering the volume of the regions, the ROMs of the third model have all been made with parameters that have a relatively inflated importance. Most of these parameters are part of the side reflector region, as this region is the largest in the geometry of the third model.

The thesis demonstrated the feasibility of applying the nonintrusive POD technique on the neutronics model of the U-Battery, and to additionally use perturbation theory to select the most important parameters. The method has shown to alleviate computational cost significantly for all examined models. However, the upfront cost of building the reduced models by sampling the high-fidelity models has been considerable, especially when evaluating the resulting accuracy. A proper selection of the POD tolerances must be made to ensure sufficient accuracy and to prevent oversampling. Combining the POD technique with perturbation theory showed to be a promising way of selecting only a few parameters for participation in the ROM building. The high number of available parameters gets diminished to only the ones that are most important to the output of the model, resulting in less sampling while ensuring the resulting ROM to be as accurate as possible.

6.1 Recommendations

The first recommendation for further use of the proposed method is to build the ROMs iteratively. Each iteration, the tolerances can be lowered to remedy the sensible problem of the POD tolerances. Following this procedure, eventually the right tolerances can be found that result in a ROM with sufficient accuracy, while preventing oversampling by immediately setting the tolerances too small. The evaluations can be saved to prevent recalculations of the same parameter settings each iteration, such that no computational resources will be lost.

A second recommendation is for analyzing changes to either the whole reflector or fuel regions. In this case, sensitivities gathered by the GPT module should be summed for all the regions that belong to either the reflector or fuel part of the reactor core, because the sensitivities are determined only for local changes. Summation is valid because the sensitivity values are linearly approximated, and the summed values show the influence of changing material properties of either the whole fuel or reflector part.

Lastly, for further research to improve the method of combining perturbation theory with the adaptive POD technique, a reduced adjoint approach is recommended [27]. The adjoint of the reduced model itself may be calculated during the building phase of the ROM, and sensitivities of the parameters can then be computed quickly for any point in the parameter space. The sensitivities can now be used to determine for each parameter if it needs more sampling and which points in the parameter space it should include in the next iteration of the building phase. This would improve the adaptive POD technique by reducing oversampling significantly.

Bibliography

[1] P.A. Arias, N. Bellouin, E. Coppola, R.G. Jones, G. Krinner, J. Marotzke, V. Naik, M.D. Palmer, G.-K. Plattner, J. Rogelj, et al. Climate Change 2021: The Physical Science Basis. Contribution of Working Group I to the Sixth Assessment Report of the Intergovernmental Panel on Climate Change; Technical Summary. *The Intergovernmental Panel on Climate Change AR6*, 2021.

[2] Eurostat. Shedding light on energy in the EU. https://ec.europa.eu/eurostat/cache/infographs/energy/, 2022. [Online; accessed 23-July-2022].

[3] S. Lorenczik, S. Kim, B. Wanner, J. M. Bermudez Menendez, U. Remme, T. Hasegawa, J. H. Keppler, L. Mir, G. Sousa, M. Berthelemy, et al. Projected costs of generating electricity-2020 edition. Technical report, Organisation for Economic Co-Operation and Development, 2020.

[4] L. Byers, J. Friedrich, R. Hennig, A. Kressig, X. Li, L. M. Valeri, and C. McCormick. A Global Database of Power Plants. *World Resources Institute*, 2018.

[5] L Adamovich, S Banerjee, M Bolshunkhin, E Budylov, M Chaki IV Dulera, P Fomichnko, K Furukawa, B Gabaraev, and E Greenspan. Status of small reactor designs without on-site refueling. *IAEA-TECDOC-1536, IAEA*, 2007.

[6] T. McLaughlin. Creaky U.S. power grid threatens progress on renewables, EVs. https://www.reuters.com/investigates/special-report/usa-renewables-electric-grid/, 2022. [Online; accessed 23-July-2022].

[7] M. Ding and J. L. Kloosterman. Parametric neutronics design of a small and long-life htr. *Proceedings of HTR*, 2010, 2010.

[8] M. Ding and J. L. Kloosterman. Thermal-hydraulic design and transient evaluation of a small long-life htr. *Nuclear engineering and design*, 255:347–358, 2013.

[9] S. H. Begg, M. B. Welsh, and R. B. Bratvold. Uncertainty vs. Variability: What's the Difference and Why is it Important? In *SPE Hydrocarbon Economics and Evaluation Symposium*. OnePetro, 2014.

[10] F. D'Auria, N. Muellner, C. Parisi, and A. Petruzzi. BEPU approach in licensing framework, including 3D NK applications. *New Trends in Technologies: Devices, Computer, Communication, and Industrial Systems*, 2010.

[11] P. Benner, S. Gugercin, and K. Willcox. A survey of projection-based model reduction methods for parametric dynamical systems. *SIAM review*, 57(4):483–531, 2015.

[12] W. H. A. Schilders, H. A. Van der Vorst, and J. Rommes. *Model order reduction: theory, research aspects and applications*, volume 13. Springer, 2008.

[13] Y.C. Liang, H.P. Lee, S.P. Lim, W.Z. Lin, K.H. Lee, and C.G. Wu. Proper orthogonal decomposition and its applications - Part I: Theory. *Journal of Sound and Vibration*, 252(3):527–544, 2002.

[14] M. Van den Berg. *High-Fidelity Multi-Physics Modelling of the U-Battery Nuclear Microreactor*. PhD thesis, first year report. Delft University of Technology, 2022.

[15] D. G. Cacuci. *Sensitivity and Uncertainty Analysis, Volume I: Theory*. CRC Press, 2003.

[16] J. van Kan, A. Segal, and F. J. Vermolen. *Numerical methods in scientific computing*. VSSD, 2005.

[17] S. Hamid, T. Kolev, Q. T. Le Gia, and W. Wu. Numerical solution of partial differential equations using wavelet approximation space. *Math*, 667:1–28, 2000.

[18] M. Eldred and D. Dunlavy. Formulations for surrogate-based optimization with data fit, multifidelity, and reduced-order models. In *11th AIAA/ISSMO Multidisciplinary Analysis and Optimization Conference*, 2006.

[19] F. Alsayyari. *Adaptive data-driven reduced-order modelling techniques for nuclear reactor analysis*. PhD thesis, Delft University of Technology, 2020.

[20] F. Alsayyari, M. Tiberga, Z. Perkó, D. Lathouwers, and J. L. Kloosterman. A nonintrusive adaptive reduced order modeling approach for a molten salt reactor system. *Annals of Nuclear Energy*, 141:107321, 2020.

[21] M. L. Williams. *Handbook of Nuclear Reactors Calculations, III*. CRC Press, 1986.

[22] J. Leppänen, M. Pusa, T. Viitanen, V. Valtavirta, and T. Kaltiaisenaho. The serpent monte carlo code: Status, development and applications in 2013. *Annals of Nuclear Energy*, 82:142–150, 2015.

[23] M. Tiberga, D. Lathouwers, and J. L. Kloosterman. A discontinuous Galerkin FEM multiphysics solver for the Molten Salt Fast Reactor. In *International Conference on Mathematics and Computational Methods applied to Nuclear Science and Engineering (M&C 2019), Portland, OR, USA*, 2019.

[24] T. A. Wareing, J. M. McGhee, J. E. Morel, and S. D. Pautz. Discontinuous finite element SN methods on three-dimensional unstructured grids. *Nuclear science and engineering*, 138(3):256–268, 2001.

[25] Fahad Alsayyari, Zoltán Perkó, Danny Lathouwers, and Jan Leen Kloosterman. A nonintrusive reduced order modelling approach using proper orthogonal decomposition and locally adaptive sparse grids. *Journal of Computational Physics*, 399:108912, 2019.

[26] W. A. Klimke. *Uncertainty modeling using fuzzy arithmetic and sparse grids*. Citeseer, 2006.

[27] M. U. Altaf, M. El Gharamti, A. W. Heemink, and I. Hoteit. A reduced adjoint approach to variational data assimilation. *Computer Methods in Applied Mechanics and Engineering*, 254:1–13, 2013.

Appendix

A.1 Parameters k_{eff} model 3

Table A1: Parameters considered for the k_{eff} of model three with their nominal values. Region 1099, 1100 and 1401 are the bottom, side, and top reflector regions, respectively, and regions 2XYY indicate fuel block layer X and symmetric elements containing fuel block YY, following Figure 3.1. Group one is the fast group.

Parameter	Nominal value $[cm^{-1}]$	Parameter	Nominal value $[cm^{-1}]$
$\Sigma_{s,2}^{1100}$	3.17×10^{-1}	$\Sigma_{s,2}^{1099}$	3.19×10^{-1}
$\Sigma_{s,15}^{1100}$	4.93×10^{-1}	$\Sigma_{s,2}^{1401}$	3.19×10^{-1}
$\Sigma_{s,14}^{1100}$	4.80×10^{-1}	$\Sigma_{c,7}^{2201}$	3.33×10^{-3}
$\Sigma_{s,13}^{1100}$	4.78×10^{-1}	$\Sigma_{c,7}^{2301}$	3.33×10^{-3}
$\Sigma_{s,7}^{1100}$	4.75×10^{-1}	$\Sigma_{c,7}^{2202}$	3.33×10^{-3}
$\Sigma_{s,6}^{1100}$	4.75×10^{-1}	$\Sigma_{c,7}^{2302}$	1.61×10^{-4}
$\Sigma_{s,3}^{1100}$	4.58×10^{-1}	$\Sigma_{c,14}^{1100}$	3.33×10^{-3}
$\Sigma_{s,5}^{1100}$	4.74×10^{-1}	$\Sigma_{c,9}^{2208}$	8.14×10^{-3}
$\Sigma_{s,4}^{1100}$	4.72×10^{-1}	$\Sigma_{c,9}^{2308}$	8.14×10^{-3}
$\Sigma_{s,9}^{1100}$	4.75×10^{-1}	$\Sigma_{s,7}^{2201}$	3.90×10^{-1}
$\Sigma_{s,8}^{1100}$	4.75×10^{-1}	$\Sigma_{s,7}^{2301}$	3.90×10^{-1}
$\Sigma_{s,11}^{1100}$	4.76×10^{-1}	$\Sigma_{s,9}^{2208}$	3.86×10^{-1}
$\Sigma_{s,12}^{1100}$	4.77×10^{-1}	$\Sigma_{s,9}^{2308}$	3.31×10^{-4}
$\Sigma_{s,16}^{1100}$	5.12×10^{-1}	$\Sigma_{c,16}^{1100}$	3.86×10^{-1}
$\Sigma_{c,15}^{1100}$	2.20×10^{-4}	$\Sigma_{c,8}^{2201}$	6.26×10^{-3}
$\Sigma_{c,9}^{2201}$	8.15×10^{-3}	$\Sigma_{c,8}^{2301}$	6.27×10^{-3}
$\Sigma_{c,9}^{2301}$	8.14×10^{-3}	$\Sigma_{c,9}^{2101}$	8.17×10^{-3}
$\Sigma_{s,9}^{2201}$	3.86×10^{-1}	$\Sigma_{c,9}^{2401}$	3.90×10^{-1}
$\Sigma_{s,9}^{2301}$	3.86×10^{-1}	$\Sigma_{s,7}^{2202}$	8.18×10^{-3}
$\Sigma_{c,9}^{2202}$	8.14×10^{-3}	$\Sigma_{s,7}^{2302}$	3.90×10^{-1}
$\Sigma_{c,9}^{2302}$	8.14×10^{-3}	$\Sigma_{s,9}^{2101}$	3.86×10^{-1}
$\Sigma_{s,10}^{1100}$	4.75×10^{-1}	$\Sigma_{s,9}^{2401}$	3.86×10^{-1}
$\Sigma_{s,9}^{2202}$	3.86×10^{-1}	$\Sigma_{s,8}^{2201}$	3.87×10^{-1}
$\Sigma_{s,9}^{2302}$	3.86×10^{-1}	$\Sigma_{s,8}^{2301}$	6.27×10^{-3}
$\Sigma_{s,1}^{1100}$	1.53×10^{-1}	$\Sigma_{c,8}^{2202}$	3.88×10^{-1}

A.2 Sensitivities $k_{\mathbf{eff}}$ model 3

Table A2: The top 50 sensitivity values of the k_{eff} for the 17 group model for a one-percent perturbation in the cross section data at a nominal k_{eff} of 1.3186. Region 1099, 1100 and 1401 are the bottom, side, and top reflector regions, respectively, and regions 2XYY indicate fuel block layer X and symmetric elements containing fuel block YY, following Figure 3.1. Group one is the fast group.

Parameter	Sensitivity [pcm]	Region	Reaction	Group
$\Sigma_{s,2}^{1100}$	11.2	1100	scatter	2
$\Sigma_{s,15}^{1100}$	5.39	1100	scatter	15
$\Sigma_{s,14}^{1100}$	5.07	1100	scatter	14
$\Sigma_{s,13}^{1100}$	4.97	1100	scatter	13
$\Sigma_{s,7}^{1100}$	4.88	1100	scatter	7
$\Sigma_{s,6}^{1100}$	4.37	1100	scatter	6
$\Sigma_{s,3}^{1100}$	4.03	1100	scatter	3
$\Sigma_{s,5}^{1100}$	3.49	1100	scatter	5
$\Sigma_{s,4}^{1100}$	3.47	1100	scatter	4
$\Sigma_{s,9}^{1100}$	3.33	1100	scatter	9
$\Sigma_{s,8}^{1100}$	2.73	1100	scatter	8
$\Sigma_{s,11}^{1100}$	2.62	1100	scatter	11
$\Sigma_{s,12}^{1100}$	2.04	1100	scatter	12
$\Sigma_{s,16}^{1100}$	1.82	1100	scatter	16
$\Sigma_{c,15}^{1100}$	−1.67	1100	capture	15
$\Sigma_{c,9}^{2201}$	−1.65	2201	capture	9
$\Sigma_{c,9}^{2301}$	−1.64	2301	capture	9
$\Sigma_{s,9}^{2201}$	1.55	2201	scatter	9
$\Sigma_{s,9}^{2301}$	1.55	2301	scatter	9
$\Sigma_{c,9}^{2202}$	−1.46	2202	capture	9
$\Sigma_{c,9}^{2302}$	−1.46	2302	capture	9
$\Sigma_{s,10}^{1100}$	1.45	1100	scatter	10
$\Sigma_{s,9}^{2202}$	1.38	2202	scatter	9
$\Sigma_{s,9}^{2302}$	1.38	2302	scatter	9
$\Sigma_{s,1}^{1100}$	1.31	1100	scatter	1
$\Sigma_{s,2}^{1099}$	1.28	1099	scatter	2
$\Sigma_{s,2}^{1401}$	1.28	1401	scatter	2
$\Sigma_{c,7}^{2201}$	−1.15	2201	capture	7
$\Sigma_{c,7}^{2301}$	−1.15	2301	capture	7
$\Sigma_{c,7}^{2202}$	−1.02	2202	capture	7
$\Sigma_{c,7}^{2302}$	−1.02	2302	capture	7
$\Sigma_{c,14}^{1100}$	−1.02	1100	capture	14
$\Sigma_{c,9}^{2208}$	−1.00	2208	capture	9
$\Sigma_{c,9}^{2308}$	−1.00	2308	capture	9
$\Sigma_{s,7}^{2201}$	0.970	2201	scatter	7

Table A2 (continued).

Parameter	Sensitivity [pcm]	Region	Reaction	Group
$\Sigma_{s,7}^{2301}$	0.969	2301	scatter	7
$\Sigma_{s,9}^{2208}$	0.951	2208	scatter	9
$\Sigma_{s,9}^{2308}$	0.950	2308	scatter	9
$\Sigma_{c,16}^{1100}$	−0.948	1100	capture	16
$\Sigma_{c,8}^{2201}$	−0.909	2201	capture	8
$\Sigma_{c,8}^{2301}$	−0.91	2301	capture	8
$\Sigma_{c,9}^{2101}$	−0.88	2101	capture	9
$\Sigma_{c,9}^{2401}$	−0.88	2401	capture	9
$\Sigma_{s,7}^{2202}$	0.87	2202	scatter	7
$\Sigma_{s,7}^{2302}$	0.86	2302	scatter	7
$\Sigma_{s,9}^{2101}$	0.83	2101	scatter	9
$\Sigma_{s,9}^{2401}$	0.83	2401	scatter	9
$\Sigma_{s,8}^{2201}$	0.83	2201	scatter	8
$\Sigma_{s,8}^{2301}$	0.83	2301	scatter	8
$\Sigma_{c,8}^{2202}$	−0.81	2201	capture	8

A.3 Parameters R_f model 3

Table A3: Parameters considered for the fission reaction rate detector of model three with their nominal values. Region 1100 and 1401 are the side and top reflector, respectively, region 2201 is the center fuel region considered in Equation (3.1), and group one is the fast group.

Parameter	Nominal value $[cm^{-1}]$	Parameter	Nominal value $[cm^{-1}]$
$\Sigma^{1100}_{s,13}$	4.78×10^{-1}	$\Sigma^{2201}_{s,11}$	3.86×10^{-1}
$\Sigma^{2201}_{f,15}$	8.34×10^{-3}	$\Sigma^{1401}_{s,2}$	3.19×10^{-1}
$\Sigma^{2201}_{f,13}$	5.28×10^{-3}	$\Sigma^{1100}_{s,11}$	4.76×10^{-1}
$\Sigma^{2201}_{f,14}$	5.74×10^{-3}	$\Sigma^{2201}_{f,12}$	2.97×10^{-3}
$\Sigma^{2201}_{f,16}$	1.34×10^{-2}	$\Sigma^{1401}_{s,15}$	4.93×10^{-1}
$\Sigma^{1100}_{s,15}$	4.93×10^{-1}	$\Sigma^{2201}_{s,9}$	3.86×10^{-1}
$\Sigma^{1100}_{s,14}$	4.80×10^{-1}	$\Sigma^{2201}_{f,7}$	1.03×10^{-3}
$\Sigma^{1100}_{s,12}$	4.77×10^{-1}	$\Sigma^{1401}_{s,14}$	4.80×10^{-1}
$\Sigma^{2201}_{s,2}$	2.53×10^{-1}	$\Sigma^{2201}_{s,7}$	3.90×10^{-1}
$\Sigma^{1401}_{s,13}$	4.78×10^{-1}	$\Sigma^{2201}_{s,6}$	3.87×10^{-1}

A.4 Sensitivities R_f model 3

Table A4: The top 20 sensitivity values of the fission reaction rate detector response for the 17 group model for a one-percent perturbation in the cross section data at a nominal response value of 9.77×10^{-3}. Region 1100 and 1401 are the side and top reflector, respectively, region 2201 is the center fuel region considered in Equation (3.1), and group one is the fast group.

Parameter	Sensitivity [%]	Region	Reaction	Group
$\Sigma^{1100}_{s,13}$	1.78×10^{-1}	1100	scatter	13
$\Sigma^{2201}_{f,15}$	1.77×10^{-1}	2201	fission	15
$\Sigma^{2201}_{f,13}$	1.28×10^{-1}	2201	fission	13
$\Sigma^{2201}_{f,14}$	1.23×10^{-1}	2201	fission	14
$\Sigma^{2201}_{f,16}$	8.70×10^{-2}	2201	fission	16
$\Sigma^{1100}_{s,15}$	8.48×10^{-2}	1100	scatter	15
$\Sigma^{1100}_{s,14}$	7.96×10^{-2}	1100	scatter	14
$\Sigma^{1100}_{s,12}$	5.80×10^{-2}	1100	scatter	12
$\Sigma^{2201}_{s,2}$	5.47×10^{-2}	2201	scatter	2
$\Sigma^{1401}_{s,13}$	5.15×10^{-2}	1401	scatter	13
$\Sigma^{2101}_{s,11}$	4.86×10^{-2}	2201	scatter	11
$\Sigma^{1401}_{s,2}$	4.73×10^{-2}	1401	scatter	2
$\Sigma^{1100}_{s,11}$	4.20×10^{-2}	1100	scatter	11
$\Sigma^{2201}_{f,12}$	4.18×10^{-2}	2201	fission	12
$\Sigma^{1401}_{s,15}$	4.16×10^{-2}	1401	scatter	15
$\Sigma^{2201}_{s,9}$	3.99×10^{-2}	2201	scatter	9
$\Sigma^{2201}_{f,7}$	3.75×10^{-2}	2201	fission	7
$\Sigma^{1401}_{s,14}$	3.70×10^{-2}	1401	scatter	14
$\Sigma^{2201}_{s,7}$	3.51×10^{-2}	2201	scatter	7
$\Sigma^{2201}_{s,6}$	3.49×10^{-2}	2201	scatter	6